Implementation and evaluation of the shifted fracture method for crack propagation in fiber-reinforced polymer composites

Stijn Anton Platzer

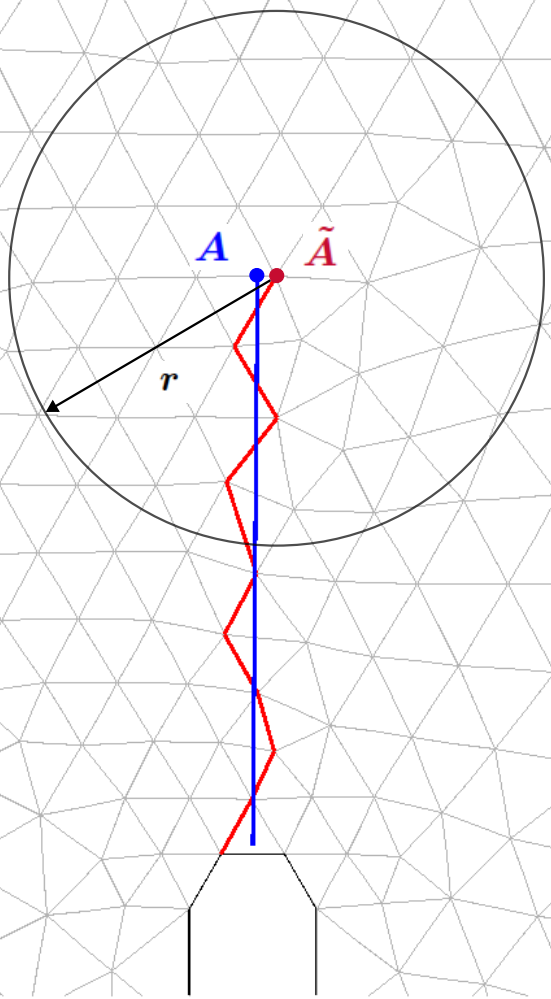

TU Delft

Implementation and evaluation of the shifted fracture method for crack propagation in fiber-reinforced polymer composites

by

Stijn Anton Platzer

to obtain the degree of Master of Science
at the Delft University of Technology,
to be defended publicly on Thursday February 6, 2025 at 09:00 AM.

Student number:	5135486	
Project duration:	August 5, 2024 – February 6, 2025	
Thesis committee:	Dr. ir. F. P. van der Meer,	TU Delft, supervisor
	Dr. ir. O. J. Colomés Gené,	TU Delft
	Ir. P. Hofman,	TU Delft

Style: TU Delft Report Style, with modifications by Daan Zwaneveld

An electronic version of this thesis is available at `http://repository.tudelft.nl/`.

TU Delft

Preface

I present my master's thesis, in which I have implemented and evaluated the shifted fracture method (SFM), a newly proposed method for arbitrary crack propagation, and explored its application to fiber-reinforced polymer (FRP) composites. These materials have advantageous properties, but predicting crack propagation remains a significant challenge due to their complex failure behavior. Therefore, this thesis investigates whether the SFM can be used as an alternative to the currently used model for micromechanical analysis.

During my master's studies in civil engineering, I was particularly fascinated by courses covering complex analysis methods and simulations, especially those involving the finite element method. I have always found the full understanding and application of such methods very engaging, particularly when they can be used to solve real-world problems. For me, the most rewarding part of the entire process is translating theory into practical results and simulations, as this provides valuable insights into how cracks propagate and can be modeled in complex materials, such as FRP composites.

Like any research project, this thesis was not without its challenges. One of the biggest obstacles was the implementation of the SFM. As the SFM is a recently published method with limited information available, I had to base most of my implementation on a single research paper. Additionally, I was tasked with integrating the SFM into the existing in-house finite element code. The major challenge here was that the code was written in C++, a programming language I had never used before. However, I was eager to take on these challenges, and through patience, asking questions, and a step-by-step approach, I successfully implemented the method to a great extent. One of the key milestones was developing a reduced version of the SFM that achieved nearly the same results as the full implementation but with lower computational complexity.

I could not have completed this thesis without the support of others. First, I would like to thank my supervisors, Dr. Ir. F. P. van der Meer and Dr. Ir. O. J. Colomés Gené, for their valuable insights and assistance in understanding the method. A special word of thanks goes to Ir. P. Hofman, my daily supervisor. The weekly meetings helped me to stay on schedule and discover new ideas and solutions. I appreciate the time my supervisors invested in helping me navigate the complexities of this topic.

Ultimately, I hope these insights on the SFM will lay the groundwork for future research and contribute to the further development of the SFM for advanced materials, such as FRP composites.

Stijn Anton Platzer
Delft, January 2025

Summary

Fiber-reinforced polymer (FRP) composites are used in various engineering applications due to their many advantageous properties, but predicting failure remains challenging due to their complex failure behavior. The Computational Mechanics group at TU Delft uses an inter-element cohesive zone method, referred to as the Ortiz model, to analyze crack propagation at the microscale. Although the method can successfully predict complex failure processes in FRP composites, it is highly mesh-dependent, making large-scale simulations impractical.

This research implements and evaluates the shifted fracture method (SFM) as an alternative to reduce mesh dependency without significantly increasing computational complexity. Its effectiveness is investigated through a step-by-step implementation to systematically investigate the importance of its main components and compare it with the Ortiz model. The SFM introduces some key modifications, including an area correction term in the crack boundary terms, an adapted crack propagation algorithm, shifted weak form equations, and shifted cohesive zone conditions, which are shifted using Taylor expansions. To explore the importance of these key components, three versions were tested: (1) the full SFM implementation, (2) a reduced SFM with only the area correction term and crack propagation algorithm, and (3) an extended Ortiz model with only the area correction term.

Numerical simulations show that the reduced SFM is robust, computationally efficient, and mesh-independent in basic fracture simulations. Based on these findings, further testing was conducted using this model instead of the full SFM. The results confirm the importance of the area correction term in reducing mesh dependency. The extended Ortiz model, on the other hand, showed less accurate results in predicting cracks, even though this version does correct for the effective crack surface area. Furthermore, the criterion used to determine the crack direction, the maximum principal tensile stress, proved unsuitable for mixed-mode fracture scenarios and led to inaccurate crack paths.

Although the reduced SFM is promising for basic fracture tests, the method, in its current form, is not yet directly applicable to complex fracture scenarios, such as in FRP composites. To improve this, additional features, including crack initiation, merging, and termination, were implemented. These features show promising results in basic fracture tests; however, further validation of these features and the implementation of additional features are needed to make the reduced SFM suitable for FRP composites. This research concludes that the reduced SFM is a computationally efficient and mesh-independent solution for basic fracture testing, but additional refinements are needed for complex fracture scenarios. Therefore, recommendations are made on what is needed for extending the SFM for more complex fracture scenarios and FRP composites.

Contents

1

Introduction

Fiber-reinforced polymer (FRP) composites are used in various engineering applications due to their exceptional properties, such as lightweight, high strength-to-weight ratio, corrosion resistance, and versatility. The advantageous properties of FRP composites are mainly due to their multiscale nature. However, this multiscale nature introduces significant challenges in understanding and predicting the failure behavior of FRP composites [1].

Failure in FRP composites often involves complex, interacting mechanisms such as densely distributed cracking caused by matrix cracking and fiber-matrix debonding. Furthermore, fiber breakage can occur, as well as complex failure processes such as crack merging and branching. Failure analysis of composite structures must account for all possible processes as well as their interactions. Predicting the initiation of these failure processes alone is often not sufficient, as local damage usually does not lead to the immediate collapse of the structure. Therefore, the failure analysis must be progressive, which means that the progression of failure in the material must be simulated. These complex failure behaviors make it challenging to accurately model the progressive failure behavior of FRP composites. Mesoscale modeling offers computational efficiency by homogenizing the fibers and polymer matrix. However, these models often fail to capture essential micromechanical interactions that are crucial for understanding complex fracture processes [2]. On the other hand, micromechanical modeling provides a much more detailed physics-based representation, but its high computational costs make large-scale simulations impractical.

An ideal solution would be a fully coupled multiscale failure analysis, where detailed local simulations inform the global structural response [1]. For this, there remains a huge challenge in developing computational models at the microscale that are capable of simulating results both quickly and accurately.

Over time, various computational methods have been developed to predict and analyze crack propagation at the microscale. At TU Delft, the Computational Mechanics group uses an inter-element cohesive zone method. In this method, cohesive elements are dynamically inserted along the element boundaries when a stress-based failure criterion is met. This technique, originally introduced by Ortiz and Camacho [3], is referred to in this research as the ”Ortiz model”. Crack initiation in the Ortiz model starts at the middle node of edges of six-noded triangular elements by splitting the nodes and inserting a cohesive element. To ensure a smooth response and avoid singularities, the model uses a shifted cohesive law [4], which ensures that traction at zero crack opening matches the cohesive traction at crack initiation.

The Ortiz model has proven successful in predicting the complex failure mechanisms observed in FRP composites, such as densely distributed cracking, crack merging, and branching. This is achieved by dynamically checking all mid-nodes of the elements within the mesh and allowing cracks to initiate throughout the entire domain. Its ability to propagate multiple cracks and to simulate the interactions between these cracks makes it well-suited for capturing complex failure behavior. However, the Ortiz model is an inter-element cracking method, meaning that cracks can only propagate along the edges of the finite element mesh. This creates mesh dependency since the crack path is constrained by the mesh configuration. This dependency influences the accuracy of the results: a coarser mesh reduces

accuracy, while a finer mesh improves accuracy but significantly increases computational costs. Furthermore, cohesive zone modeling imposes requirements on element size to ensure accurate results, further contributing to computational challenges.

These limitations highlight the need for computational models that minimize mesh dependency, allowing for accurate results even with coarser mesh sizes. Such models can significantly lower computational costs and make large-scale simulations more practical and efficient.

In this thesis, these challenges are addressed by the implementation and evaluation of the shifted fracture method (SFM), a recently proposed framework for arbitrary crack growth. The SFM introduces several key innovations to improve the accuracy of crack propagation while maintaining computational efficiency. In this method, the fracture interface conditions are approximated using a surrogate fracture surface, which consists of the element edges of the finite element mesh that are closest to the true fracture surface. To reduce mesh dependency, the SFM shifts the fracture interface conditions using Taylor expansions, ensuring that the interface conditions on the surrogate surface closely approximate those on the true fracture surface. These Taylor expansions compensate for any differences between the surrogate and true fracture representations. Unlike traditional cohesive zone models and node-release techniques, the SFM significantly reduces mesh dependency and ensures an accurate representation of the true fracture area. It also avoids the creation of small, irregularly shaped cells (cut cells) near cracks, as seen in methods like XFEM, and thus avoids the complexities of stabilizing cracks within the finite element mesh. These advantages make the SFM a promising approach for FRP composites, where reducing mesh dependency is essential for lowering computational costs while maintaining accuracy in failure predictions.

The aim of this research project is to implement and test the SFM into an in-house finite element code for micromechanical analysis, comparing it to the Ortiz model and assessing its effectiveness for FRP composites.

The main research question of this study is:

- How effective is the proposed method for arbitrary crack growth in predicting the propagation of cracks in fiber-reinforced polymer composites?

To address this main research question, the following sub-questions are considered:

- What are the key components of the proposed crack growth prediction method?
- How does the proposed method compare to the existing Ortiz model in terms of accuracy and computational efficiency?
- How does the proposed method perform under complex crack growth scenarios observed in FRP composites?
- What are the limitations and challenges associated with the proposed method?

In this research project, the SFM is implemented step by step to systematically investigate the importance of its main components. The Ortiz model serves as the starting point for the implementation, and gradually, key components of the SFM are introduced. Throughout the implementation, various intermediate versions of the SFM are explored to better understand the significance of its key components, as well as the applicability and limitations when applied to complex fracture scenarios and FRP composites. Also, extra attention is given to challenges such as crack initialization, merging, and termination, which play a critical role in successfully modeling FRP composites.

A series of numerical simulations are performed to evaluate the performance of the implemented versions of the SFM in comparison to the Ortiz model. All the simulations are performed in two dimensions under the plane strain assumption, using the finite element method (FEM) to implicitly solve the quasi-static equilibrium equation. The analyses are based on fracture mechanics principles, with a particular focus on crack path accuracy in both simple and complex geometries. The research is structured into four key phases:

1. **Implementation:** developing and implementing the SFM into the in-house finite element code.
2. **Verification and validation:** testing the accuracy and computational efficiency through benchmark tests and experimental data.
3. **Testing simplified approach:** exploring the feasibility of a reduced-complexity version of the SFM.
4. **Application of additional features:** extending the method to enhance its applicability for FRP composites.

The structure of this thesis is organized as follows: Chapter 2 outlines the theoretical background, covering key concepts in FRP composites, cohesive zone modeling, and the theoretical frameworks of both the Ortiz model and the SFM. Chapter 3 details the implementation process, addressing the challenges encountered in applying the SFM to FRP composites and the implementation of additional features. Chapter 4 presents the results, starting with the verification and validation of the complete SFM implementation, along with a partially implemented version on basic cases, followed by an evaluation of an even further simplified version of the SFM and an analysis of the effects of crack initialization, merging, and termination. Chapter 5 discusses the findings, limitations, and recommendations for future work. Finally, Chapter 6 wraps up the thesis and summarizes key outcomes.

2

Theoretical Background

This chapter presents the theoretical background for this thesis. Starting with an overview of fiber-reinforced polymer (FRP) composites, explaining their multiscale nature, failure mechanisms at the microscale, and limitations and challenges. After that, the basics of cohesive zone modeling (CZM) are explained. This is done because of its fundamental role in both the Ortiz model and the shifted fracture method (SFM). After that, the Ortiz model is explained in detail, where the crack propagation process, the shifted cohesive law, and the numerical solutions scheme are explained. Also, the limitations of the model are discussed, such as mesh dependency and the computational challenges. To address these challenges, the SFM is introduced, aimed at reducing mesh dependency, improving accuracy, and enhancing computational efficiency. Finally, a theoretical comparison between the Ortiz model and the SFM is made to establish a good starting point for the numerical implementation discussed in the following chapter.

2.1. Fiber-reinforced polymer (FRP) composites

FRP composites consist of high-strength fibers embedded in a polymer matrix. Due to their many advantages, such as high-strength-to-weight ratio, durability, and versatility, FRP composites are used in various engineering applications. The fibers are typically made of materials such as glass, carbon, aramid, or basalt [5] and carry most of the load. The matrix is usually composed of thermoset or thermoplastic resin, which keeps the fibers in place and ensures load transfer between the fibers and matrix. Different composite designs exist, such as woven, braided, and non-crimp fabric configurations. But, the most commonly used design is the traditional laminate composite, which is made of unidirectional plies. Here, the fibers are aligned in a fixed orientation within each ply, and multiple plies with varying fiber orientations are placed on top of each other. This makes it easy to adjust the material properties to the specific application.

The advantageous properties of FRP composites are mainly due to their multiscale nature (see Figure 2.1), which contributes to their exceptional mechanical properties. However, the multiscale nature also introduces significant challenges in understanding and predicting their behavior [1]. The following section investigates the multiscale nature of FRP composites and their implications for fracture modeling.

2.1.1. Multiscale nature of FRP composites

Laminated FRP composites have a multiscale nature, which means that the mechanical behavior can be analyzed at different scales. These three different scales include (see Figure 2.1):

- **Microscale:** At this scale, the structure of the composite is detailed, where the individual fibers and the surrounding matrix material can be distinguished. This scale will be considered in this thesis.
- **Mesoscale:** In this scale, the plies within the composite are homogenized to an orthotropic material. The fiber orientation influences the ply properties.
- **Macroscale:** At the largest scale, the whole laminate composite is considered as a single equivalent material, with properties obtained through thickness homogenization.

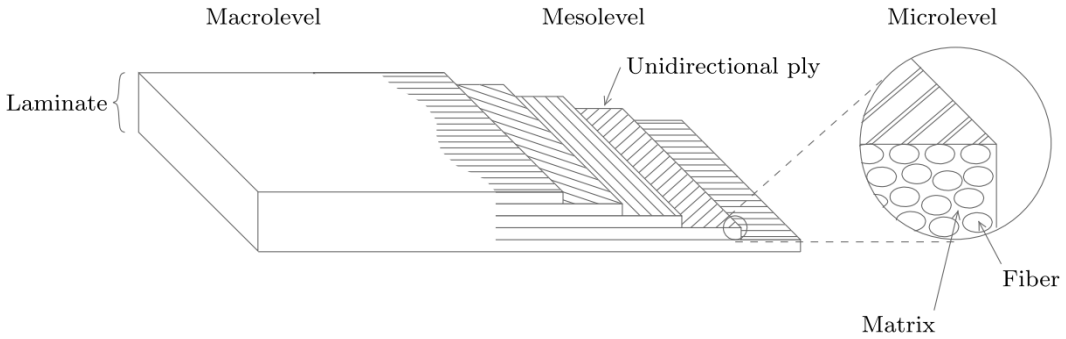

Figure 2.1: Three levels of observation for a composite laminate [1].

Mesoscale modeling offers computational efficiency because the fibers and the polymer matrix are homogenized. However, they often cannot capture critical microscale interactions, which influences the failure behavior [2]. Micromechanical modeling, on the other hand, can provide a more detailed representation but also requires more computational costs. This makes the application to large-scale simulations often not possible. The ideal solution would be a fully coupled multiscale failure analysis, where detailed local simulations dynamically inform the global structural response [1].

2.1.2. Failure mechanisms in FRP composites at the microscale

In FRP composites, there are different failure mechanisms that are all important for predicting the behavior of composites. Failure in FRP composites usually involves multiple interacting processes. At the microscale, these are:

- **Matrix cracking:** Cracks develop in the polymer matrix due to localized stress concentrations.
- **Fiber breakage or kinking:** Fibers may fracture under tensile loading or buckle and kink under compressive forces.
- **Fiber-matrix debonding:** The interface between the fibers and matrix detaches, disrupting stress transfer and causing localized damage.

Usually, predicting the initiation of failure is not sufficient because failures, such as matrix cracking, do not necessarily compromise the structural integrity of the composite. When matrix failure occurs, the load-bearing capacity is maintained through stress redistribution to the fibers. So, to accurately predict the behavior of composites, progressive failure modeling must be considered. This allows the simulation of stress redistribution and the evolution of damage after initial failure [1].

2.1.3. Limitations and challenges

Despite the many advantages, the use of FRP composites in engineering practice is set back due to challenges in understanding and modeling the failure behavior. Because of the complex failure mechanisms, ensuring structural safety often relies on extensive and expensive experimental testing. If reliable computational models were available, simulations could replace some physical tests, reducing costs and enabling better optimization of materials and designs. However, this remains a key challenge because current computational methods experience a trade-off between accuracy and computational cost, particularly for microscale simulations [1].

So, there lies a major challenge in developing models that are capable of accurately predicting crack propagation and are also computationally efficient. While micro-simulations can capture progressive damage and complex fiber-matrix interactions, the computational costs remain a problem. To address this, this thesis focuses on improving microscale analysis for both accuracy and computational efficiency in crack propagation prediction.

2.2. Cohesive zone modelling

Cohesive zone models (CZM) are widely used in fracture mechanics for simulating material separation and fracturing processes. This concept was first introduced by Dugdale [6] and Barenblatt [7]. In CZMs, a thin zone that vanishes ahead of the crack tip, known as the cohesive zone, is introduced. This cohesive zone effectively eliminates stress singularities and controls energy dissipation during crack propagation. It consists of upper and lower surfaces referred to as cohesive surfaces, which are held together by cohesive tractions. These tractions resist separation and are governed by a cohesive law that relates the cohesive tractions $\boldsymbol{t}$ to the size of the displacement jump of the cohesive surfaces $[\![\boldsymbol{u}]\!]$ [1]:

$$\boldsymbol{t} = \boldsymbol{t}([\![\boldsymbol{u}]\!]) \tag{2.1}$$

Figure 2.2 illustrates a cohesive zone ahead of a crack tip with the cohesive surfaces held together by cohesive tractions $\boldsymbol{t}$. Figure 2.3 shows a general cohesive law, illustrating the relationship between cohesive traction $\boldsymbol{t}$ and the displacement jump $[\![\boldsymbol{u}]\!]$. This cohesive law can be described as follows [8]:

$$\boldsymbol{t} = \boldsymbol{t}_{max}\boldsymbol{f}\left(\frac{[\![\boldsymbol{u}]\!]}{[\![\boldsymbol{u}]\!]_{max}}\right) \tag{2.2}$$

where $\boldsymbol{t}_{max}$ is the maximum cohesive traction, $[\![\boldsymbol{u}]\!]_{max}$ is a characteristic separation displacement, and $\boldsymbol{f}$ is a dimensionless function describing the shape of the cohesive traction-separation curve (cohesive curve) depending on the failure mechanism. A variety of cohesive laws exist to describe material behavior. In this thesis, a shifted cohesive law 2.6 is used, which will be detailed in the next section.

Another important material parameter of the CZM is the fracture energy $\boldsymbol{G}_f$ [9]:

$$\boldsymbol{G}_f = \int_0^{[\![\boldsymbol{u}]\!]_{max}} \boldsymbol{t}([\![\boldsymbol{u}]\!])d[\![\boldsymbol{u}]\!] \tag{2.3}$$

This integral represents the total energy dissipated during crack propagation, corresponding to the area under the cohesive traction-separation curve (see Figure 2.3).

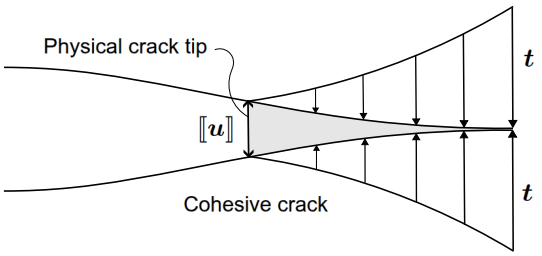

Figure 2.2: Cohesive zone ahead of a crack tip. Modified from [8].

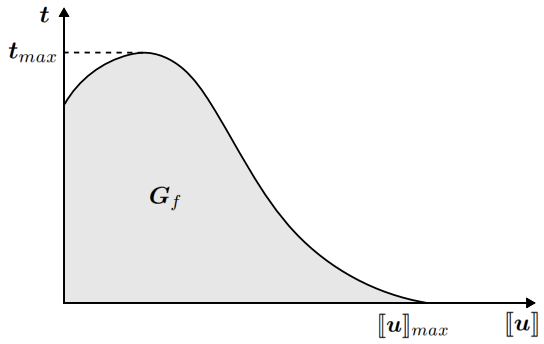

Figure 2.3: General cohesive law describing the relationship between the cohesive traction and the separation displacement. Modified from [8].

The CZM plays a key role in this thesis, as both the Ortiz model and the SFM rely on CZMs to simulate fracture propagation. This section lays out the foundational principles of CZMs, which are essential for understanding both the Ortiz model and the SFM.

2.3. The Ortiz model: inter-element cohesive zone method

In Section 2.1, a brief introduction was provided on fiber-reinforced polymer composites, which experience complex failure processes at the microscale. Over time, various computational methods have been developed to predict and analyze crack propagation at this scale. The Computational Mechanics group at TU Delft uses an inter-element cohesive zone method, referred to as the Ortiz model, in this thesis. In this method, cohesive elements are dynamically inserted along the element boundaries when a stress-based failure criterion is met, as originally described by Ortiz and Camacho [3].

2.3.1. Crack propagation in the Ortiz model

Crack initiation in the Ortiz model occurs at the middle node of the edges of six-noded triangular elements. When a stress-based failure criterion is met, the nodes are split, and a cohesive element is inserted (see Figure 2.4). The stress-based failure criterion is defined as [3]:

$$\sigma^{\text{eff}} \geq f_t, \quad \text{where} \quad \sigma^{\text{eff}} = \begin{cases} \sqrt{(t_n)^2 + \theta(|t_s|)^2}, & \text{if } [\![u]\!]_n \geq 0 \\ \sqrt{\theta(|t_s| - \mu|t_n|)}, & \text{if } [\![u]\!]_n < 0 \end{cases} \tag{2.4}$$

where $\mathbf{f}_t$ is the cohesive strength, $\boldsymbol{\sigma}^{\text{eff}}$ the effective stress, $t = (t_n, t_s)$ the traction of cohesive surface along the normal direction and shear direction in the local n, s frame (see Figure 2.5), $[\![u]\!] = ([\![u]\!]_n, [\![u]\!]_s)$ the displacement jump along normal and shear direction, θ a shear stress factor, and μ the friction coefficient.

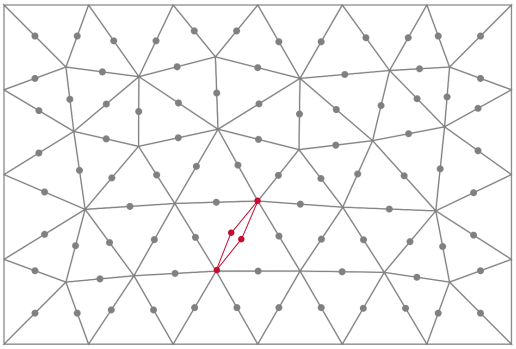

Figure 2.4: Sketch of the dynamic insertion technique of cohesive elements

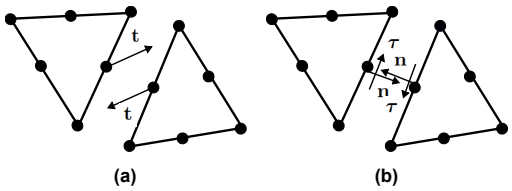

Figure 2.5: (a) Mid node traction forces $\mathbf{t}$. (b) Normal and shear stresses $\mathbf{n}$ and $\boldsymbol{\tau}$.

Once the criterion for cohesive element insertion is met, the crack path is determined by solving the discretized quasi-static equilibrium equation, which accounts for the traction forces acting on the cohesive edges. [10]

2.3.2. The shifted cohesive law

Cohesive elements are inserted dynamically during the simulation. To keep the results smooth and prevent singularities, the cohesive law needs to be carefully designed. For example, if the cohesive traction has a non-zero value at zero crack opening, directly applying this can lead to singularities under mixed-mode loading conditions (See Figure 2.6 (left)). [11]

To address this, the shifted cohesive law is adopted. In this approach, the displacement jump $[\![\boldsymbol{u}]\!]$ across the crack is shifted by a value that depends on the magnitude of the displacement jump at crack initiation as proposed by Hille et al. [4] (see Figure 2.6 (middle)):

$$[\![\boldsymbol{u}]\!]^{shifted} = [\![\boldsymbol{u}]\!] + [\![\boldsymbol{u}]\!]^0 \tag{2.5}$$

where the shift $[\![\boldsymbol{u}]\!]^0$ is defined as:

$$[\![\boldsymbol{u}]\!]^0 = \frac{t^0}{K_m} \tag{2.6}$$

in which t^0 is the cohesive traction at the moment of crack initiation and K_m is the initial dummy stiffness.

This shift ensures that the cohesive law behaves as if it has an initially rigid response, avoiding artificial compliance while maintaining numerical stability. As shown in Figure 2.6 (right), the traction-separation relation is shifted such that the traction at zero crack opening matches the cohesive traction at crack initiation.[2, 12]

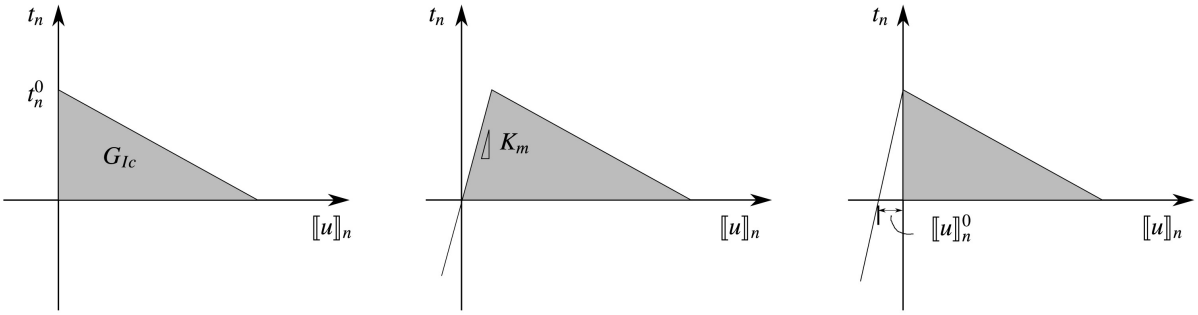

(a) Initially rigid (b) Initially stiff (c) Shifted origin

Figure 2.6: Pure mode I representation of shift in cohesive law to mimic initially rigid behavior [1].

2.3.3. Numerical solution scheme

The Ortiz model uses the Newton-Raphson method as an incremental-iterative solver for solving the system of equations in finite element analysis [13]. This method iteratively reduces the unbalance at each load increment to achieve equilibrium. To handle the complex equilibrium paths associated with progressive failure in composite materials, such as snap-back behavior, the equilibrium path is traced using a combination of displacement-control and the dissipation-based arc-length method, as described by Gutiérrez [14]. This approach is detailed in [1], with a brief summary provided below.

Failure in composites often involves sharp snap-backs along the equilibrium path, particularly when matrix failure occurs. Two simultaneous processes contribute to this behavior: matrix material damage and fiber unloading. Fiber unloading releases a significant amount of elastic energy, which can exceed the energy required to drive matrix damage, resulting in unstable damage growth, and snap-back behavior is observed. To address these challenges, the dissipation-based arc-length method is used. In this method, a fixed amount of energy dissipation is prescribed per step, enabling stable progression along the equilibrium path. Figure 2.7 illustrates how the equilibrium path is incrementally followed using equal energy dissipation steps. However, this method only works when energy dissipation occurs; during purely elastic stages, the system becomes singular.

To overcome this limitation, a hybrid loading strategy is adopted. The simulation begins with displacement-controlled analysis (Figure 2.8) during elastic stages and switches to dissipation-based arc-length control when damage initiates and energy dissipation becomes significant. The solver also incorporates an adaptive increment size strategy to recover from non-convergence, ensuring continuity of the analysis.

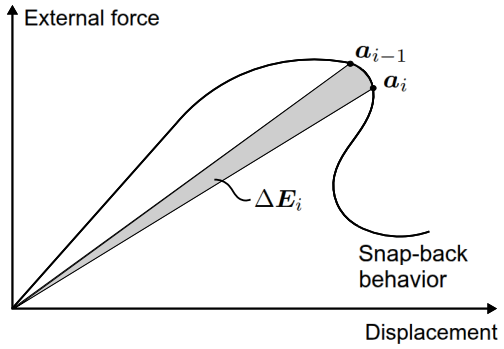

Figure 2.7: Incremental solution of the equilibrium path using the dissipation-based arc-length method during damage evolution.

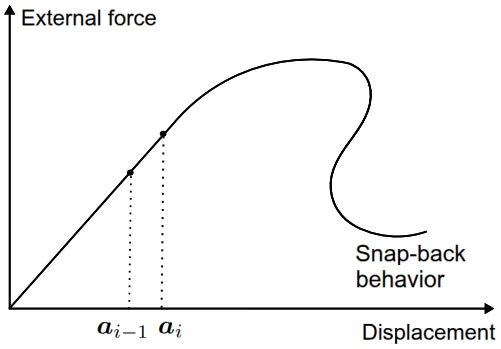

Figure 2.8: Incremental solution of the equilibrium path using displacement-controlled analysis during elastic stages.

In summary, the Ortiz model's numerical solution scheme combines displacement control and dissipation-based arc-length control to trace complex equilibrium paths, including snap-back behavior and post-failure responses. For a detailed explanation of this solution scheme, readers are referred to [1], with further details on the dissipation-based arc-length method available in [14].

2.3.4. Limitations of the Ortiz model

The Ortiz model has proven to be an effective method for predicting crack growth in composite materials. Failure processes such as densely distributed cracking, crack merging, and branching can be well simulated with this model, as it allows crack initiation throughout the entire domain. It also allows different cracks to merge or close. However, the method also has some notable limitations, which come from the fact that the Ortiz model is an inter-element cracking method, which means that cracks can only grow along the element boundaries of the finite element mesh. Furthermore, the method relies on the cohesive zone model, which introduces its own challenges. The following key limitations highlight the method's challenges and the improvements that are needed:

1. **Mesh dependency**
   The Ortiz model is dependent on the mesh configuration, as cracks are constrained to grow along the edges of the finite elements. This influences the following aspects:
   - **Accuracy:** A coarser mesh reduces accuracy because the crack path is restricted to predefined element edges, which may not align with the actual crack path.
   - **Computational costs:** A finer mesh improves accuracy by better approximating the crack path but significantly increases computational costs.
2. **Overestimation of the fracture energy**
   In the Ortiz model, cracks are only allowed to grow along existing element edges, which can lead to an overestimation of fracture energy. This can happen when the actual crack path does not match the mesh geometry. This introduces mesh bias, which can only be compensated by remeshing. [9]
3. **Element size requirements**
   Robust and accurate simulations require element sizes to be several times smaller than the cohesive zone length. This limits the applicability of the Ortiz model to small-scale simulations, and large-scale computations are not feasible due to rapidly escalating computational costs. [1]

These limitations demonstrate the need for a more robust computational framework that can reduce mesh dependency, allowing cracks to develop independently of the mesh configuration. This would reduce computational costs, which is beneficial for large-scale simulations or three-dimensional simulations. To address these limitations and challenges, the following section presents a novel approach to arbitrary crack propagation: the shifted fracture method (SFM) proposed by Li et al. [15, 16].

2.4. The shifted fracture method (SFM): a novel approach

The shifted fracture method (SFM), introduced by Li et al. [15, 16], is a novel approach for modeling crack propagation. In this method, the true fracture surface is approximated by a surrogate fracture surface, which consists of element edges along the crack path in the finite element mesh. To reduce mesh dependency, the SFM shifts the fracture interface conditions using Taylor expansions, ensuring that the interface conditions on the surrogate surface closely approximate those on the true fracture surface. These Taylor expansions compensate for discrepancies between the surrogate and true fracture representations.

2.4.1. Key features and innovations

The SFM introduces several innovative features that can improve crack modeling while maintaining computational efficiency. The method offers simplicity and computational data structures comparable to techniques such as node-release techniques (NRT) [17], but with the accuracy of methods like extended finite element methods (XFEM) [18] and generalized finite element methods (GFEM) [19]. This allows for the prediction of complex crack propagation with high accuracy and without the complicated computational structure often associated with advanced techniques. The SFM introduces the following innovative features to improve crack modeling [15, 16]:

- **Accurate representation of fracture area:** The SFM correctly accounts for the area of the true fracture. This can be observed in the variational equations, where projection terms map the surrogate fracture surface onto the true fracture surface.

- **Reduction of mesh dependency:** Unlike classical cohesive zone models or node-release/element-deletion techniques, the SFM reduces the severe mesh dependencies typically observed by shifting the fracture interface conditions using Taylor expansions, ensuring that the interface conditions on the surrogate surface closely approximate those on the true fracture surface. The Taylor expansions compensate for any differences between the surrogate and true fracture representations.
- **Application of Taylor expansions:** Cohesive fracture models are well suited for Taylor expansions, as they naturally prevent stress singularities near the fracture tip, ensuring numerical stability.
- **Sharp interface modeling with simple implementation:** The SFM behaves as a sharp interface model, providing accuracy comparable to XFEM and GFEM while maintaining simpler data structures and integration rules. Unlike XFEMs and GFEMs, which can create small, irregularly shaped cells (cut cells) near cracks, the SFM avoids the creation of such cut cells. Cut cells often need extra numerical stabilization techniques to handle small elements, which can complicate the implementation and increase computational costs. By completely avoiding the generation of cut cells, the SFM eliminates the need for stabilization mechanisms, leading to a simpler and more robust numerical implementation.
- **Computational efficiency:** The selection of the crack propagation direction and the update of the fracture surface in the SFM have computational complexities similar to node-release techniques (NRT). Consequently, the necessary data structures and algorithms are comparable to those in NRT-based methods.

2.4.2. Theoretical framework

This section presents the key theoretical foundations of the SFM. The formulation begins with the governing equations for a fracturing elastic solid, followed by their weak form representation. Fundamental concepts such as true and surrogate cracks are introduced, forming the basis for the development of the shifted cohesive zone conditions. Finally, the derivation of the shifted weak form equations is discussed, which plays a crucial role in the SFM framework. [15, 16]

Governing equations for a fracturing elastic solid

The basic governing equations for a fracturing elastic solid under small deformation are first introduced [20]. Consider a domain $\Omega \subset R^2$ with boundary $\Gamma \equiv \partial\Omega$. A single crack, denoted by Γ_c divides the domain into two subdomains Ω^m where $m = \pm$ such that $\Omega = \Omega^+ \cup \Omega^-$ (see Figure 2.9). The rest of the boundary Γ is further divided into dirichlet and neumann boundaries for each subdomain, denoted as Γ_u^m and Γ_t^m, respectively. Before fracture, the displacement field remains continuous across Γ_c. However, once a failure criterion is met, a discontinuity in the displacement field is introduced to model crack propagation. The governing equations for this problem are:

$$-\nabla \cdot \boldsymbol{\sigma}^m = \boldsymbol{b}^m, \quad \text{in } \Omega^m, \tag{2.7}$$

$$\boldsymbol{\sigma}^m \cdot \boldsymbol{n}^m = \bar{\boldsymbol{t}}^m, \quad \text{on } \Gamma_N^m, \tag{2.8}$$

$$\boldsymbol{u}^m = \overline{\boldsymbol{u}}^m, \quad \text{on } \Gamma_D^m, \tag{2.9}$$

$$\boldsymbol{t} \equiv \boldsymbol{t}^+ = \boldsymbol{\sigma}^+ \cdot \boldsymbol{n}^+ = -\boldsymbol{\sigma}^- \cdot \boldsymbol{n}^- = -\boldsymbol{t}^-, \quad \text{on } \Gamma_c, \tag{2.10}$$

$$\boldsymbol{t} = \boldsymbol{t}_{coh}(\llbracket \boldsymbol{u} \rrbracket), \quad \text{on } \Gamma_c. \tag{2.11}$$

The first equality is enforcing the balance of forces, where σ is the stress tensor, ∇ is the gradient operator, and b is the (volumetric) body force. The next two conditions are the prescribed traction and displacement boundary conditions $\bar{\boldsymbol{t}}^m$ and $\overline{\boldsymbol{u}}^m$, respectively. The last two conditions are associated with the crack interface where $\boldsymbol{n}^+$ and $\boldsymbol{n}^-$ are the outward unit normals to Ω^+ and Ω^-, respectively, $\boldsymbol{t}_{coh}(\llbracket \boldsymbol{u} \rrbracket)$ is the cohesive traction vector to be defined by a cohesive law and $\llbracket \boldsymbol{u} \rrbracket$ the displacement jump.

For elastic materials under the small strain assumption, the constitutive equation is given by:

$$\boldsymbol{\sigma} = \boldsymbol{C} : \boldsymbol{\varepsilon} \tag{2.12}$$

where the strain tensor reads $\boldsymbol{\varepsilon} = \nabla^s \boldsymbol{u} = \frac{1}{2}(\nabla \boldsymbol{u} + \nabla^T \boldsymbol{u})$ defined as the symmetric gradient of the displacement field $\boldsymbol{u}$ and $\boldsymbol{C}$ is the fourth-order elastic stiffness tensor. For linear isotropic elastic materials,

the elastic stiffness tensor is written as:

$$C_{ijkl} = \lambda\delta ij\delta kl + \mu(\delta ik\delta jl + \delta il\delta jk) \tag{2.13}$$

where $\lambda = \frac{E\nu}{(1+\nu)(1-2\nu)}$ and $\mu = \frac{E}{2(1+\nu)}$ are the Lame constants, E the Young's modulus, ν the Poisson's ratio and δ_{ij} is the Kronecker delta tensor.

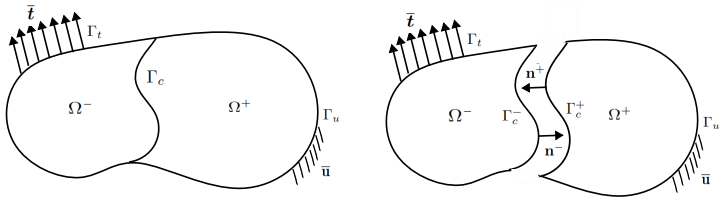

Figure 2.9: Domain with an internal interface crack.

Weak form equations

To derive the weak form equations from the equilibrium equation (Eq. 2.7), the equation is multiplied by the test functions $\boldsymbol{w}^+$ and $\boldsymbol{w}^-$. Integrating the resulting expression over the domain yields the following formulation [21]:

$$-\sum_{m=\pm}^{2}\int_{\Omega}\boldsymbol{w}^m\cdot(\nabla\cdot\boldsymbol{\sigma}^m)\,\mathrm{d}\Omega = \sum_{m=\pm}^{2}\int_{\Omega}\boldsymbol{w}^m\cdot\boldsymbol{b}^m\;\mathrm{d}\Omega \quad\forall\quad \boldsymbol{w}^m \tag{2.14}$$

Applying integration by parts or the divergence theorem yields the weak form equation:

$$\sum_{m=\pm}^{2}\int_{\Omega}\nabla^s\boldsymbol{w}^m:\boldsymbol{\sigma}^m\,\mathrm{d}\Omega = \sum_{m=\pm}^{2}\int_{\Omega}\boldsymbol{w}^m\cdot\boldsymbol{b}^m\;\mathrm{d}\Omega + \sum_{m=\pm}^{2}\int_{\Gamma}\boldsymbol{w}^m\cdot(\boldsymbol{\sigma}^m\cdot\boldsymbol{n}^m)\;\mathrm{d}\Gamma \quad\forall\quad \boldsymbol{w}^m \tag{2.15}$$

Substitution of the neumann and crack boundary conditions gives the weak form equation:

$$\begin{aligned}\sum_{m=\pm}^{2}\int_{\Omega}\nabla^s\boldsymbol{w}^m:\boldsymbol{\sigma}^m\,\mathrm{d}\Omega + \int_{\Gamma_c}\boldsymbol{w}^+\cdot(\boldsymbol{\sigma}^+\cdot\boldsymbol{n}^+)\;\mathrm{d}\Gamma + \int_{\Gamma_c}\boldsymbol{w}^-\cdot(\boldsymbol{\sigma}^-\cdot\boldsymbol{n}^-)\;\mathrm{d}\Gamma \\ = \sum_{m=\pm}^{2}\int_{\Omega}\boldsymbol{w}^m\cdot\boldsymbol{b}^m\;\mathrm{d}\Omega + \sum_{m=\pm}^{2}\int_{\Gamma_N}\boldsymbol{w}^m\cdot\bar{\boldsymbol{t}}^m\;\mathrm{d}\Gamma \quad\forall\quad \boldsymbol{w}^m\end{aligned} \tag{2.16}$$

This weak form equation can be rewritten in another form by using the following equality:

$$\boldsymbol{\sigma}^+\cdot\boldsymbol{n}^+\cdot\boldsymbol{w}^+ + \boldsymbol{\sigma}^-\cdot\boldsymbol{n}^-\cdot\boldsymbol{w}^- = [\![\boldsymbol{w}]\!]\cdot\{\!\{\boldsymbol{\sigma}\}\!\}\cdot\boldsymbol{n} + \{\!\{\boldsymbol{w}\}\!\}\cdot[\![\boldsymbol{\sigma}]\!]\cdot\boldsymbol{n} \tag{2.17}$$

where the two crack boundary terms are expressed into a mean value and a jump value using the operators $\{\!\{\cdot\}\!\}$ and $[\![\cdot]\!]$, respectively:

$$\begin{aligned}\{\!\{\boldsymbol{w}\}\!\} &= \frac{1}{2}(\boldsymbol{w}^+ + \boldsymbol{w}^-), & [\![\boldsymbol{w}]\!] &= \boldsymbol{w}^+ - \boldsymbol{w}^-,\\ \{\!\{\boldsymbol{\sigma}\}\!\}\cdot\boldsymbol{n} &= \frac{1}{2}(\boldsymbol{\sigma}^+ + \boldsymbol{\sigma}^-)\boldsymbol{n}, & [\![\boldsymbol{\sigma}]\!]\cdot\boldsymbol{n} &= (\boldsymbol{\sigma}^+ - \boldsymbol{\sigma}^-)\boldsymbol{n}.\end{aligned}$$

In this thesis, it is assumed that the material on either side of the fracture is the same, so λ-weighted average $\{\!\{x\}\!\}_\lambda = \lambda x^+ + (1-\lambda)x^-$ is set to 1/2 in the numerical computations. This can be changed when there are big differences in material properties or mesh sizes across the crack interface.

Proof: on Γ_c we have

$$\begin{aligned}
\boldsymbol{\sigma}^+ \cdot \boldsymbol{n}^+ \cdot \boldsymbol{w}^+ + \boldsymbol{\sigma}^- \cdot \boldsymbol{n}^- \cdot \boldsymbol{w}^- =& \boldsymbol{\sigma}^+ \cdot \boldsymbol{n} \cdot \boldsymbol{w}^+ - \boldsymbol{\sigma}^- \cdot \boldsymbol{n} \cdot \boldsymbol{w}^- \qquad (\boldsymbol{n}^+ = -\boldsymbol{n}^- = \boldsymbol{n}) \\
=& \frac{1}{2}(\boldsymbol{\sigma}^+ \cdot \boldsymbol{n} \cdot \boldsymbol{w}^+ + \boldsymbol{\sigma}^+ \cdot \boldsymbol{n} \cdot \boldsymbol{w}^- - \boldsymbol{\sigma}^- \cdot \boldsymbol{n} \cdot \boldsymbol{w}^+ - \boldsymbol{\sigma}^- \cdot \boldsymbol{w}^- \boldsymbol{n}) + \\
& \frac{1}{2}(\boldsymbol{\sigma}^+ \cdot \boldsymbol{n} \cdot \boldsymbol{w}^+ + \boldsymbol{\sigma}^- \cdot \boldsymbol{n} \cdot \boldsymbol{w}^+ - \boldsymbol{\sigma}^+ \cdot \boldsymbol{n} \cdot \boldsymbol{w}^- - \boldsymbol{\sigma}^- \cdot \boldsymbol{w}^- \boldsymbol{n}) \\
=& \frac{1}{2}(\boldsymbol{w}^+ + \boldsymbol{w}^-) \cdot (\boldsymbol{\sigma}^+ - \boldsymbol{\sigma}^-)\boldsymbol{n} + \frac{1}{2}(\boldsymbol{\sigma}^+ + \boldsymbol{\sigma}^-)\boldsymbol{n} \cdot (\boldsymbol{w}^+ - \boldsymbol{w}^-) \\
=& [\![\boldsymbol{w}]\!] \cdot \{\!\{\boldsymbol{\sigma}\}\!\} \cdot \boldsymbol{n} + \{\!\{\boldsymbol{w}\}\!\} \cdot [\![\boldsymbol{\sigma}]\!] \cdot \boldsymbol{n}
\end{aligned}$$

where in the first line, the equality $\boldsymbol{n}^+ = -\boldsymbol{n}^- = \boldsymbol{n}$ is used. Substitution of equality 2.17 gives the weak form equation:

$$\begin{aligned}
\sum_{m=\pm}^{2} \int_\Omega \nabla^s \boldsymbol{w}^m : \boldsymbol{\sigma}^m \, \mathrm{d}\Omega + \int_{\Gamma_c} [\![\boldsymbol{w}]\!] \cdot \{\!\{\boldsymbol{\sigma}\}\!\} \cdot \boldsymbol{n} \, \mathrm{d}\Gamma + \int_{\Gamma_c} \{\!\{\boldsymbol{w}\}\!\} \cdot [\![\boldsymbol{\sigma}]\!] \cdot \boldsymbol{n} \, \mathrm{d}\Gamma \\
= \sum_{m=\pm}^{2} \int_\Omega \boldsymbol{w}^m \cdot \boldsymbol{b}^m \, \mathrm{d}\Omega + \sum_{m=\pm}^{2} \int_{\Gamma_N} \boldsymbol{w}^m \cdot \bar{\boldsymbol{t}}^m \, \mathrm{d}\Gamma \quad \forall \quad \boldsymbol{w}^m
\end{aligned} \tag{2.18}$$

By applying the identities $[\![\boldsymbol{\sigma}]\!] \cdot \mathbf{n} = 0$ and $\{\!\{\boldsymbol{\sigma}\}\!\} \cdot \mathbf{n} = \boldsymbol{t}_{coh}$ which follows from (Eq. 2.10), the weak form equation of the Ortiz model is obtained:

$$\sum_{m=\pm}^{2} \int_\Omega \nabla^s \boldsymbol{w}^m : \boldsymbol{\sigma}^m \, \mathrm{d}\Omega + \int_{\Gamma_c} [\![\boldsymbol{w}]\!] \cdot \boldsymbol{t}_{coh} \, \mathrm{d}\Gamma = \sum_{m=\pm}^{2} \int_\Omega \boldsymbol{w}^m \cdot \boldsymbol{b}^m \, \mathrm{d}\Omega + \sum_{m=\pm}^{2} \int_{\Gamma_N} \boldsymbol{w}^m \cdot \bar{\boldsymbol{t}}^m \, \mathrm{d}\Gamma \quad \forall \quad \boldsymbol{w}^m \tag{2.19}$$

This demonstrates that the fundamental weak form equations are the same for both methods. However, in the SFM, an additional shift is introduced to modify the cohesive zone conditions. This shifted formulation will be developed in the following sections.

The true and surrogate crack

The goal of the SFM is to shift the location where the true fracture cohesive conditions are applied Γ_c to a surrogate location $\tilde{\Gamma}_c$. This is done by shifting the cohesive zone conditions and the weak form equation. The surrogate location $\tilde{\Gamma}_c$ is defined by the edges of the mesh that are closest to the true crack Γ_c using the closest point projection, where the distance vector is defined as:

$$\boldsymbol{d} = \boldsymbol{x} - \tilde{\boldsymbol{x}} \tag{2.20}$$

In Figure 2.10, an example of a finite element mesh is shown where the blue line represents the true crack Γ_c, the red line the surrogate crack $\tilde{\Gamma}_c$, and with black arrows the distance vector d at two locations along $\tilde{\Gamma}_c$ are shown.

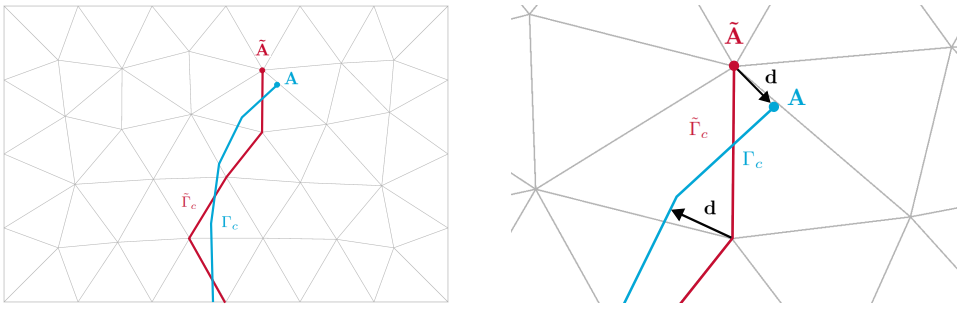

Figure 2.10: The true crack Γ_c, the surrogate crack $\tilde{\Gamma}_c$ and the distance vector d at two locations along $\tilde{\Gamma}_c$. Modified from [15].

Shifted cohesive zone conditions

To enforce the cohesive zone model on the surrogate cohesive crack $\tilde{\Gamma}_c$ rather than on the true cohesive crack Γ_c, a first-order Taylor expansion of the displacement $\boldsymbol{u}$ and stress $\boldsymbol{\sigma}(\boldsymbol{u})$ is performed at the surrogate crack $\tilde{\Gamma}_c$:

$$\boldsymbol{u}(\tilde{\boldsymbol{x}}) = \tilde{\boldsymbol{u}}(\tilde{\boldsymbol{x}}) + (\nabla\tilde{\boldsymbol{u}}\ \boldsymbol{d})(\tilde{\boldsymbol{x}}) + \boldsymbol{R}_{\tilde{\boldsymbol{u}}}(\tilde{\boldsymbol{x}}), \quad \text{on } \tilde{\Gamma}_c, \tag{2.21}$$

$$\boldsymbol{\sigma}(\tilde{\boldsymbol{x}}) = \tilde{\boldsymbol{\sigma}}(\tilde{\boldsymbol{x}}) + (\nabla\tilde{\boldsymbol{\sigma}}\ \boldsymbol{d})(\tilde{\boldsymbol{x}}) + \boldsymbol{R}_{\boldsymbol{\sigma}}(\tilde{\boldsymbol{x}}), \quad \text{on } \tilde{\Gamma}_c \tag{2.22}$$

where

- $\boldsymbol{u}(\tilde{\boldsymbol{x}})$ is the approximated displacement field at the true crack Γ_c evaluated at point $\tilde{\boldsymbol{x}}$ on $\tilde{\Gamma}_c$,
- $\tilde{\boldsymbol{u}}(\tilde{\boldsymbol{x}})$ is the displacement field at point $\tilde{\boldsymbol{x}}$ on $\tilde{\Gamma}_c$,
- $\nabla\tilde{\boldsymbol{u}}$ is the gradient of the displacement field at point $\tilde{\boldsymbol{x}}$ on $\tilde{\Gamma}_c$,
- $\mathbf{d}(\tilde{\boldsymbol{x}})$ is the distance vector from $\tilde{\Gamma}_c$ to Γ_c at point $\tilde{\boldsymbol{x}}$.

the same applies to $\boldsymbol{\sigma}$. Equation 2.11 can now be used to shift the cohesive zone model as:

$$\boldsymbol{t} = \boldsymbol{t}_{coh}(\llbracket\boldsymbol{u}(\tilde{\boldsymbol{x}})\rrbracket), \quad \text{on } \Gamma_c. \tag{2.23}$$

where

$$\llbracket\boldsymbol{u}(\tilde{\boldsymbol{x}})\rrbracket = \boldsymbol{u}^+(\tilde{\boldsymbol{x}}) - \boldsymbol{u}^-(\tilde{\boldsymbol{x}}) \tag{2.24}$$

$$= (\tilde{\boldsymbol{u}}^+(\tilde{\boldsymbol{x}}) + (\nabla\tilde{\boldsymbol{u}}^+\ \boldsymbol{d})(\tilde{\boldsymbol{x}})) - (\tilde{\boldsymbol{u}}^-(\tilde{\boldsymbol{x}}) + (\nabla\tilde{\boldsymbol{u}}^-\ \boldsymbol{d})(\tilde{\boldsymbol{x}})) \tag{2.25}$$

$$= \underbrace{(\tilde{\boldsymbol{u}}^+(\tilde{\boldsymbol{x}}) - \tilde{\boldsymbol{u}}^-(\tilde{\boldsymbol{x}}))}_{\text{Displacement jump}} + \underbrace{((\nabla\tilde{\boldsymbol{u}}^+\ \boldsymbol{d})(\tilde{\boldsymbol{x}}) - (\nabla\tilde{\boldsymbol{u}}^-\ \boldsymbol{d})(\tilde{\boldsymbol{x}}))}_{\text{Gradient displacement jump}} \tag{2.26}$$

In Figure 2.11, an overview is drawn of the components that are needed to shift the cohesive zone model.

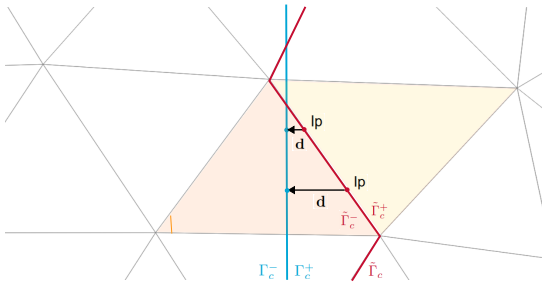

Figure 2.11: Shifting of the cohesive zone model with Taylor expansion

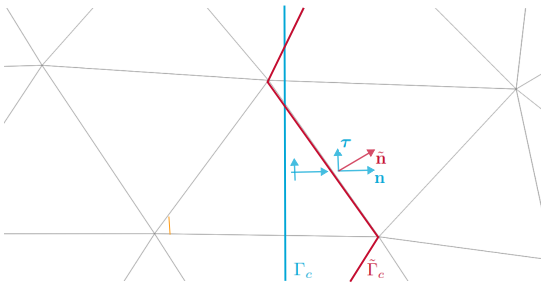

Figure 2.12: Decomposition of the normal to the surrogate crack $\tilde{\mathbf{n}}$

Higher-order interpolations could also be used, but only first-order Taylor expansions are considered in this thesis.

Shifted weak form equations

The weak form equations are shifted so that the fracture interface conditions are applied on $\tilde{\Gamma}_c$ rather than Γ_c. Therefore, Γ_c is replaced with $\tilde{\Gamma}_c$, and the normal of the true crack $\boldsymbol{n}$ is replaced with the normal of the surrogate crack $\tilde{\boldsymbol{n}}$. This results in the following weak form, where the fracture interface conditions are applied on $\tilde{\Gamma}_c$:

$$\begin{aligned}\sum_{m=\pm}^{2}\int_{\Omega}\nabla^s\boldsymbol{w}^m : \boldsymbol{\sigma}^m\ \mathrm{d}\Omega + \int_{\tilde{\Gamma}_c}\llbracket\boldsymbol{w}\rrbracket\cdot\{\!\{\boldsymbol{\sigma}\}\!\}\cdot\tilde{\boldsymbol{n}}\ \mathrm{d}\Gamma + \int_{\tilde{\Gamma}_c}\{\!\{\boldsymbol{w}\}\!\}\cdot\llbracket\boldsymbol{\sigma}\rrbracket\cdot\tilde{\boldsymbol{n}}\ \mathrm{d}\Gamma \\ = \sum_{m=\pm}^{2}\int_{\Omega}\boldsymbol{w}^m\cdot\boldsymbol{b}^m\ \mathrm{d}\Omega + \sum_{m=\pm}^{2}\int_{\Gamma_N}\boldsymbol{w}^m\cdot\bar{\boldsymbol{t}}^m\ \mathrm{d}\Gamma \quad \forall \quad \boldsymbol{w}^m\end{aligned} \tag{2.27}$$

The terms $\{\!\{\boldsymbol{\sigma}(\boldsymbol{u})\}\!\}\tilde{\boldsymbol{n}}$ and $[\![\boldsymbol{\sigma}(\boldsymbol{u})]\!]\tilde{\boldsymbol{n}}$ in equation 2.27 can be expressed in terms of shifted fracture interface conditions. The surrogate normal $\tilde{\boldsymbol{n}}$ can be decomposed in terms of its components along $\boldsymbol{n}$ and $\boldsymbol{\tau_j}$ (see Fig. 2.12):

$$\tilde{\boldsymbol{n}} = (\tilde{\boldsymbol{n}} \cdot \boldsymbol{n})\boldsymbol{n} + (\tilde{\boldsymbol{n}} \cdot \boldsymbol{\tau_j})\boldsymbol{\tau_j} \tag{2.28}$$

The term $\{\!\{\boldsymbol{\sigma}(\boldsymbol{u})\}\!\}\tilde{\boldsymbol{n}}$ can be rewritten as:

$$\begin{aligned} \{\!\{\boldsymbol{\sigma}(\boldsymbol{u})\}\!\}\tilde{\boldsymbol{n}} &= \{\!\{\boldsymbol{\sigma}(\boldsymbol{u})\}\!\}\left((\tilde{\boldsymbol{n}} \cdot \boldsymbol{n})\boldsymbol{n} + (\tilde{\boldsymbol{n}} \cdot \boldsymbol{\tau_j})\,\boldsymbol{\tau_j}\right) \\ &= (\tilde{\boldsymbol{n}} \cdot \boldsymbol{n})\,\{\!\{\boldsymbol{\sigma}(\boldsymbol{u})\}\!\}\boldsymbol{n} + (\tilde{\boldsymbol{n}} \cdot \boldsymbol{\tau_j})\{\!\{\boldsymbol{\sigma}(\boldsymbol{u})\}\!\}\boldsymbol{\tau_j} \\ &= (\tilde{\boldsymbol{n}} \cdot \boldsymbol{n})\boldsymbol{t}_{coh}(\boldsymbol{w}(\boldsymbol{u})) + \{\!\{\boldsymbol{\sigma}(\boldsymbol{u})\}\!\}(\tilde{\boldsymbol{n}} - (\tilde{\boldsymbol{n}} \cdot \boldsymbol{n})\boldsymbol{n}) \end{aligned} \tag{2.29}$$

where $\{\!\{\boldsymbol{\sigma}(\boldsymbol{u})\}\!\}\boldsymbol{n}$ can be replaced by the shifted cohesive zone model (Eq. 2.23):

$$\{\!\{\boldsymbol{\sigma}(\boldsymbol{u}(\tilde{\boldsymbol{x}}))\}\!\}\boldsymbol{n}(\tilde{\boldsymbol{x}}) = \{\!\{\boldsymbol{\sigma}(\boldsymbol{u}(\tilde{\boldsymbol{x}}))\;\boldsymbol{n}(\tilde{\boldsymbol{x}})\}\!\} \approx \boldsymbol{t}_{coh}([\![\boldsymbol{u}(\tilde{\boldsymbol{x}})]\!]) \tag{2.30}$$

Similarly, the term $[\![\boldsymbol{\sigma}(\boldsymbol{u})]\!]\tilde{\boldsymbol{n}}$ can be rewritten as:

$$\begin{aligned} [\![\boldsymbol{\sigma}(\boldsymbol{u})]\!]\tilde{\boldsymbol{n}} &= [\![\boldsymbol{\sigma}(\boldsymbol{u})]\!]\left((\tilde{\boldsymbol{n}} \cdot \boldsymbol{n})\boldsymbol{n} + (\tilde{\boldsymbol{n}} \cdot \boldsymbol{\tau_j})\,\boldsymbol{\tau_j}\right) \\ &= (\tilde{\boldsymbol{n}} \cdot \boldsymbol{n})\,[\![\boldsymbol{\sigma}(\boldsymbol{u})]\!]\boldsymbol{n} + (\tilde{\boldsymbol{n}} \cdot \boldsymbol{\tau_j})[\![\boldsymbol{\sigma}(\boldsymbol{u})]\!]\boldsymbol{\tau_j} \\ &= [\![\boldsymbol{\sigma}(\boldsymbol{u})]\!](\tilde{\boldsymbol{n}} - (\tilde{\boldsymbol{n}} \cdot \boldsymbol{n})\boldsymbol{n}) \end{aligned} \tag{2.31}$$

where the stress equilibrium condition $[\![\boldsymbol{\sigma}(\boldsymbol{u})]\!]\boldsymbol{n} = 0$ applies.

Substituting (2.29) and (2.31) into (2.27), the final shifted weak form equation for the SFM can be obtained:

$$\begin{aligned} &\sum_{m=\pm}^{2} \int_{\Omega} \nabla^s \boldsymbol{w}^m : \boldsymbol{\sigma}^m \;\mathrm{d}\Omega + \int_{\tilde{\Gamma}_c} [\![\boldsymbol{w}]\!] \cdot (\tilde{\boldsymbol{n}} \cdot \boldsymbol{n})\boldsymbol{t}_{coh}(\boldsymbol{w}(\boldsymbol{u}))\;\mathrm{d}\Gamma \\ &+ \int_{\tilde{\Gamma}_c} [\![\boldsymbol{w}]\!] \cdot \{\!\{\boldsymbol{\sigma}(\boldsymbol{u})\}\!\}(\tilde{\boldsymbol{n}} - (\tilde{\boldsymbol{n}} \cdot \boldsymbol{n})\boldsymbol{n})\;\mathrm{d}\Gamma + \int_{\tilde{\Gamma}_c} \{\!\{\boldsymbol{w}\}\!\} \cdot [\![\boldsymbol{\sigma}(\boldsymbol{u})]\!](\tilde{\boldsymbol{n}} - (\tilde{\boldsymbol{n}} \cdot \boldsymbol{n})\boldsymbol{n})\;\mathrm{d}\Gamma \\ &= \sum_{m=\pm}^{2} \int_{\Omega} \boldsymbol{w}^m \cdot \boldsymbol{b}^m \;\mathrm{d}\Omega + \sum_{m=\pm}^{2} \int_{\Gamma_N} \boldsymbol{w}^m \cdot \bar{\boldsymbol{t}}^m \;\mathrm{d}\Gamma \quad \forall \quad \boldsymbol{w}^m \end{aligned} \tag{2.32}$$

2.4.3. Theoretical comparison with the Ortiz model

This section presents a theoretical comparison of the SFM and Ortiz models to better understand their advantages and limitations. While the Ortiz model effectively captures complex failure behavior in FRP composites, it relies on inter-element crack propagation and mesh-dependent behavior, which introduces significant challenges. In contrast, the SFM offers a more flexible and computationally efficient framework by reducing mesh dependency. The following subsections present the key theoretical difference between the two methods:

Fracture representation:
An important difference between the two methods is their fracture surface representation:

- **Ortiz model:** The crack is constrained to propagate only along the edges of the finite element mesh, resulting in a less flexible and mesh-dependent representation of the fracture surface.
- **SFM:** The crack propagates along a surrogate fracture surface, which closely follows the true crack surface. This allows the crack to grow through elements, reducing mesh dependency and providing a more realistic representation of the fracture surface.

Cohesive zone conditions:
Another key difference between the two methods is how interface conditions are applied along the crack surface:

- **Ortiz model:** Interface conditions are directly applied along the edges of the finite element mesh.

- **SFM:** Instead of applying interface conditions directly on the finite element edges, the SFM shifts the interface conditions from the true crack onto the surrogate crack (finite element edges) using Taylor expansions.

Weak form equations:
The final main difference is the derivation of the weak form equations, which differs significantly between the Ortiz model and the SFM due to the introduction of shifting corrections in the SFM:

- **Ortiz model:** Standard weak form for fracturing elastic solid:

$$\int_{\Omega} \nabla^s \boldsymbol{w}^m : \boldsymbol{\sigma}^m \, \mathrm{d}\Omega + \int_{\Gamma_c} [\![\boldsymbol{w}]\!] \cdot \boldsymbol{t}_{coh} \, \mathrm{d}\Gamma = \int_{\Omega} \boldsymbol{w}^m \cdot \boldsymbol{b}^m \, \mathrm{d}\Omega + \int_{\Gamma_N} \boldsymbol{w}^m \cdot \bar{\boldsymbol{t}}^m \, \mathrm{d}\Gamma \quad \forall \quad \boldsymbol{w}^m$$

- **SFM:** The weak form introduces additional correction terms to account for the shifted interface conditions. Specifically, the SFM modifies the integral over the cohesive surface to include:
  - Area correction term $\tilde{\boldsymbol{n}} \cdot \boldsymbol{n}$ and the projection of $\tilde{\boldsymbol{n}}$ on the space of tangent vectors to the true fracture surface $\tilde{\boldsymbol{n}} - (\tilde{\boldsymbol{n}} \cdot \boldsymbol{n})\boldsymbol{n}$.
  - Stress jump and stress mean terms.

  The resulting weak form equation for the SFM reads (changes highlighted):

$$\int_{\Omega} \nabla^s \boldsymbol{w}^m : \boldsymbol{\sigma}^m \, \mathrm{d}\Omega + \int_{\tilde{\Gamma}_c} [\![\boldsymbol{w}]\!] \cdot \boxed{(\tilde{\boldsymbol{n}} \cdot \boldsymbol{n})} \boldsymbol{t}_{coh}(\boldsymbol{w}(\boldsymbol{u})) \, \mathrm{d}\Gamma + \boxed{\int_{\tilde{\Gamma}_c} [\![\boldsymbol{w}]\!] \cdot \{\!\{\boldsymbol{\sigma}(\boldsymbol{u})\}\!\}(\tilde{\boldsymbol{n}} - (\tilde{\boldsymbol{n}} \cdot \boldsymbol{n})\boldsymbol{n}) \, \mathrm{d}\Gamma}$$
$$+ \boxed{\int_{\tilde{\Gamma}_c} \{\!\{\boldsymbol{w}\}\!\} \cdot [\![\boldsymbol{\sigma}(\boldsymbol{u})]\!](\tilde{\boldsymbol{n}} - (\tilde{\boldsymbol{n}} \cdot \boldsymbol{n})\boldsymbol{n}) \, \mathrm{d}\Gamma} = \int_{\Omega} \boldsymbol{w}^m \cdot \boldsymbol{b}^m \, \mathrm{d}\Omega + \int_{\Gamma_N} \boldsymbol{w}^m \cdot \bar{\boldsymbol{t}}^m \, \mathrm{d}\Gamma \quad \forall \quad \boldsymbol{w}^m$$

  The additional projection and correction terms in the SFM improve the accuracy of crack propagation by ensuring that the surrogate fracture surface more accurately mimics the true fracture interface conditions.

In Table 2.1, a summary is given of the theoretical differences.

Table 2.1: Summary of theoretical differences between the Ortiz model and the shifted fracture method (SFM).

Aspect	Ortiz model	Shifted fracture method (SFM)
Fracture representation	Crack propagates along element edges	Crack propagates along a surrogate fracture surface following the true fracture surface
Cohesive zone conditions	Applied directly on finite element edges	Shifted from the true fracture surface onto the surrogate fracture surface using Taylor expansions
Weak form equations	Standard weak form with cohesive tractions	Modified weak form with additional projection and correction terms

This theoretical comparison highlights the fundamental differences between the Ortiz model and the SFM. While the Ortiz model provides a structured approach to crack propagation, its limitations, such as mesh dependency and fracture energy overestimation, make it less suitable for large-scale simulations. By introducing a surrogate fracture surface and applying Taylor expansions to shift interface conditions, the SFM addresses these challenges, leading to more accurate and mesh-independent fracture modeling.

In the next chapter, the numerical implementation of the SFM will be discussed in detail, highlighting how these theoretical differences are incorporated into the finite element framework.

3

Methods

This chapter details the implementation and development of the shifted fracture method (SFM) into an existing finite element code, with a particular focus on its application to fiber-reinforced polymer (FRP) composites. The methodology is structured in a stepwise manner to systematically investigate the significance of its key components.

The chapter begins by introducing the in-house finite element code and the Ortiz model, which form the foundation for the implementation. Next, the crack propagation algorithm, shifting of the cohesive zone conditions, and weak form equations are presented, which form the core components of the SFM framework. Following this, two partially implemented versions of the method are briefly introduced. These partial implementations are used alongside the complete implementation to analyze the importance of the main components and to gain a deeper understanding of the applicability and limitations of the SFM when applied to complex fracture scenarios and FRP composites. The challenges associated with applying the SFM to FRP composites are also explored. Specific attention is given to issues such as crack merging and crack initialization, as these are critical to successfully modeling FRP composites.

3.1. Implementation of the SFM

To implement the shifted fracture method (SFM) into the existing in-house finite element code, modifications were made to key functions of the Ortiz model. This section first presents an overview of the in-house finite element code before detailing how the differences between the two methods, identified in Section 2.1, are incorporated. After that, the Ortiz model will be examined, followed by an explanation of the required modifications and additions necessary to achieve the desired functionality.

For this implementation, the terminology from the original SFM paper has been slightly adapted. The term 'surrogate crack' remains unchanged and refers to tilde notations ($\tilde{\Gamma}$). However, instead of using 'true crack' as in the original formulation, this thesis simply refers to it as 'the crack' without a tilde notation (Γ). This convention is used throughout this section to improve readability and prevent confusion.

3.1.1. Overview of the in-house finite element code

The goal of this implementation is to integrate the SFM into the existing in-house finite element code written in C++, which utilizes the Jem and Jive libraries developed by Dynaflow Research Group. This code follows a structured framework where solution algorithms can be decoupled from models, ensuring flexibility and reusability. This decoupling is implemented through the following building blocks [22]:

- **Modules:** Implement the solution algorithms; they determine the execution steps of the program.
- **Models:** Implement the equations to be solved; they specify how each step is executed.

This structure allows solution algorithms to be reused across different models, ensuring robustness and adaptability. Both the existing finite element code and the SFM can handle snap-back behaviors in equilibrium paths. While SFM introduces a Newton-Raphson method with crack opening arc-length control, the existing code employs a hybrid strategy combining displacement control and a dissipation-based

arc-length method (see Section 2.3.3). Since both approaches effectively track complex equilibrium paths, the existing solution algorithm is retained, simplifying the SFM implementation.

Because solution algorithms and models are independent, implementing the SFM only requires modifying the models while keeping the solution algorithm unchanged.
The finite element code follows a tree-like model structure, where models may contain sub-models responsible for specific computational tasks. Figure 3.1 illustrates the structure, which includes the following key components:

- **MatrixModel:** creates MatrixBuilder objects for assembling global matrices.
- **MultiModel:** encapsulates multiple child models, building block for constructing model trees.
- **OrtizModel:** implements inter-element cracks that are inserted on the fly (see Section 2.3.1).
- **DispArclenModel:** implements a hybrid displacement and arc-length control strategy, designed for use with the FlexArclenModule for robust path-following solutions (see Section 2.3.3).
- **LoadDispModel:** Handles outputting load-displacement data for specific node groups.

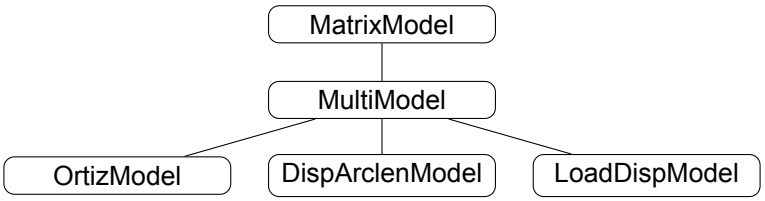

Figure 3.1: Tree structure of models used in the finite element code.

The execution order within this structure is determined by the arrangement of child models, ensuring that key operations are executed in the correct sequence.

From Section 2.4.3, it became evident that the key differences between the SFM and the existing finite element framework primarily concern the Ortiz model, which governs crack propagation. Consequently, modifications to the Ortiz model are required to integrate these differences into the finite element code. The following subsection details the necessary adjustments to the Ortiz model for implementing the SFM within the existing framework.

3.1.2. Starting point: The Ortiz model

From the previous subsection, it was established that the solution algorithm and other models remain unchanged. Thus, the implementation of the SFM requires modifications only to the Ortiz model, specifically within the OrtizModel.cpp file. The workflow of the Ortiz model consists of three main steps:

1. **Checking failure:** Identifying failure in the middle-edge nodes of triangular elements once cohesive strength is reached, based on a stress-based failure criterion (handled by `checkCommit_`, `checkFailure_`, and `checkFailureNstress_` functions).
2. **Cohesive element insertion:** Inserting new cohesive elements once cohesive strength is reached (handled by the `splitEdge_` function).
3. **Assembling of stiffness matrices and force vectors** Constructing matrices and force vectors for bulk and cohesive element (handled by `getMatrixBulk_` and `getMatrixCoh_`functions, respectively).

These steps are executed through `takeAction` functions, which are called by modules when they need data from a model. In the Ortiz model, two primary `takeAction` functions are responsible for executing these steps:

- `GET_MATRIX0 || GET_INT_VECTOR`
- `CHECK_COMMIT`

Each `takeAction` function calls specific sub-functions, which handle various computational tasks. To implement the SFM, modifications are required within these functions. Table 3.1 provides an overview of the `takeAction` functions and their corresponding sub-functions, highlighting the functions that need modifications (light grey).

Table 3.1: Overview of the `takeAction` functions in the Ortiz model, highlighting the functions that need modifications (light grey).

(a) `takeAction`: `GET_MATRIX0 || GET_INT_VECTOR`

Function	Purpose	Status
`getMatrixBulk_`	Assembles bulk stiffness matrices and force vectors.	Same
`getMatrixCoh_`	Assembles cohesive element stiffness matrices and force vectors.	Needs to be changed
`getMatrixGlue_`	Assembles glue stiffness matrices and force vectors.	Same

(b) `takeAction`: `CHECK_COMMIT`

Function	Purpose	Status
`CheckCommit_`	Contains the functions `CheckFailure_` and `splitEdge_`.	Needs to be changed
`CheckFailure_`	Checks failure criteria for mid nodes and contains `CheckFailureNStress_` function.	Needs to be changed
`CheckFailureNStress_`	Calculates failure based on stress data.	Needs to be changed
`splitEdge_`	Splits an edge, updates node data, add cohesive element connectivity and initialize material points.	Same

From Table 3.1, two major modifications are required:

- **Modification of `checkCommit_`:** The functions within `checkCommit_` must be replaced with the SFM crack propagation algorithm. Specifically, `CheckFailure_` and `CheckFailureNStress_` needs to be changed. However, `splitEdge_`, which handles the insertion of cohesive elements insertion, remains unchanged.
- **Extension of `getMatrixCoh_`:** This function must be modified to incorporate Taylor expansions to shift the cohesive zone conditions from the crack to the surrogate crack and implement the linearized discrete form of the shifted weak form equations.

The following sections provide a detailed explanation of these modifications, focusing on the new crack propagation algorithm and shifting of the cohesive zone conditions and weak form equations.

3.1.3. Crack propagation algorithm

In the Ortiz model, crack propagation relies on identifying the middle nodes of edges where the cohesive strength is exceeded and inserting cohesive elements at those edges (see Section 2.3.1). However, the SFM follows a different approach, where crack propagation is tracked using an iterative algorithm. This requires computing the crack propagation direction at each step based on the maximum tensile principal stress and incrementally extending the crack tip.

The crack propagation algorithm implemented in this thesis differs slightly from the original formulation presented in [15]. These modifications were made to simplify implementation and ensure compatibility with the existing in-house framework. Nevertheless, the key principles and computational steps remain consistent with the original SFM method. The crack propagation algorithm consists of the following steps:

Step 1: Crack initialization: Based on the predefined crack tip A_0, the initial surrogate crack tip $\tilde{A}_0$ is selected as the closest boundary node.

Step 2: Checking failure: At each time step, the current crack tips are evaluated against a stress-based failure criterion [3] to determine whether the cohesive strength has been reached. This failure criterion is directly adopted from the Ortiz model (see Section 2.3.1), ensuring consistency with the existing framework.

Step 3: Selecting the crack propagation direction: If a crack tip reaches the cohesive strength, the crack propagation direction $\boldsymbol{e}_c$ is determined. The maximum principal tensile stress criterion is used, assuming that the crack propagates orthogonally to the maximum principal stress. To improve accuracy near the crack tip, a weighted average of the stress is computed within a predefined circular region of radius $\boldsymbol{l}$ (see Figure 3.2a). Within this circular region, the stresses are calculated at the quadrature points ($\boldsymbol{q}_1, \boldsymbol{q}_2$, etc.) and used to compute the weighted average. The principal stresses are determined via eigenvalue decomposition of the weighted stress tensor $\boldsymbol{\sigma}(\boldsymbol{A})$ at the crack tip [23].

Step 4: Propagation of the crack: Once the crack direction is determined, the crack tip $\boldsymbol{A}$ is incremented along this direction by a predefined length. A new circular region of radius $\boldsymbol{r}$ is defined around the crack tip, guiding further propagation along $\boldsymbol{e}_c$ (see Figure 3.2b).

Step 5: Selecting the surrogate edges: In this step, the surrogate crack is updated by selecting the edges closest to the crack. This process consists of the following steps: (illustrated in Figures 3.2b, 3.2c, and 3.2d:

(a) Identify the set of nodes connected to the surrogate crack tip $\tilde{A}_0$ (see Figure 3.2b).
(b) Define a subset of these connected nodes for which the condition $\boldsymbol{e}_c \cdot \boldsymbol{e}(\boldsymbol{N}_*) > 0$ is satisfied. This requirement ensures that the surrogate crack propagates only forward.
(c) Calculate the distance $\boldsymbol{d}$ from each node in the subset to the half-line emanating from the crack tip in the direction $\boldsymbol{e}_c$. Select the node with the smallest distance (highlighted in red in Figure 3.2c).
(d) Add the corresponding edge to the surrogate crack and update the surrogate crack tip to this node (see Figure 3.2d).
(e) Repeat these steps until the selected node lies outside the predefined circular region.

Figure 3.3 shows the crack path and crack propagation circle at different stages of crack propagation for a vertical crack path developing upwards.

To implement this crack propagation algorithm into the Ortiz model, new functions were implemented, and some existing functions were modified. The key additions include:

- `initializeCrackHistories_` (step 1):
  - Initializes the `crackHistory` class, which tracks crack branches.
  - Sets the predefined crack tip coordinates.
  - Determines the initial surrogate node using `getClosestNodeToCrackTip_`.
  - Assigns a unique crack ID to each crack branch.
- `checkCrackPropagation_` (step 2):
  - Evaluates stresses at the crack tip to determine whether the crack can propagate.
  - Calls two primary functions:
    * `computeStressesInCircle_` (step 3):
      · Computes stresses within a circular region around the crack tip using a weighted averaging method.
      · Determines the maximum principal tensile stress and computes the crack propagation direction orthogonal to this stress.
    * `crackPropagation_` (steps 4 and 5):
      · Propagates the crack tip along the computed direction.
      · Update the surrogate crack by selecting the closest mesh edges to the crack.

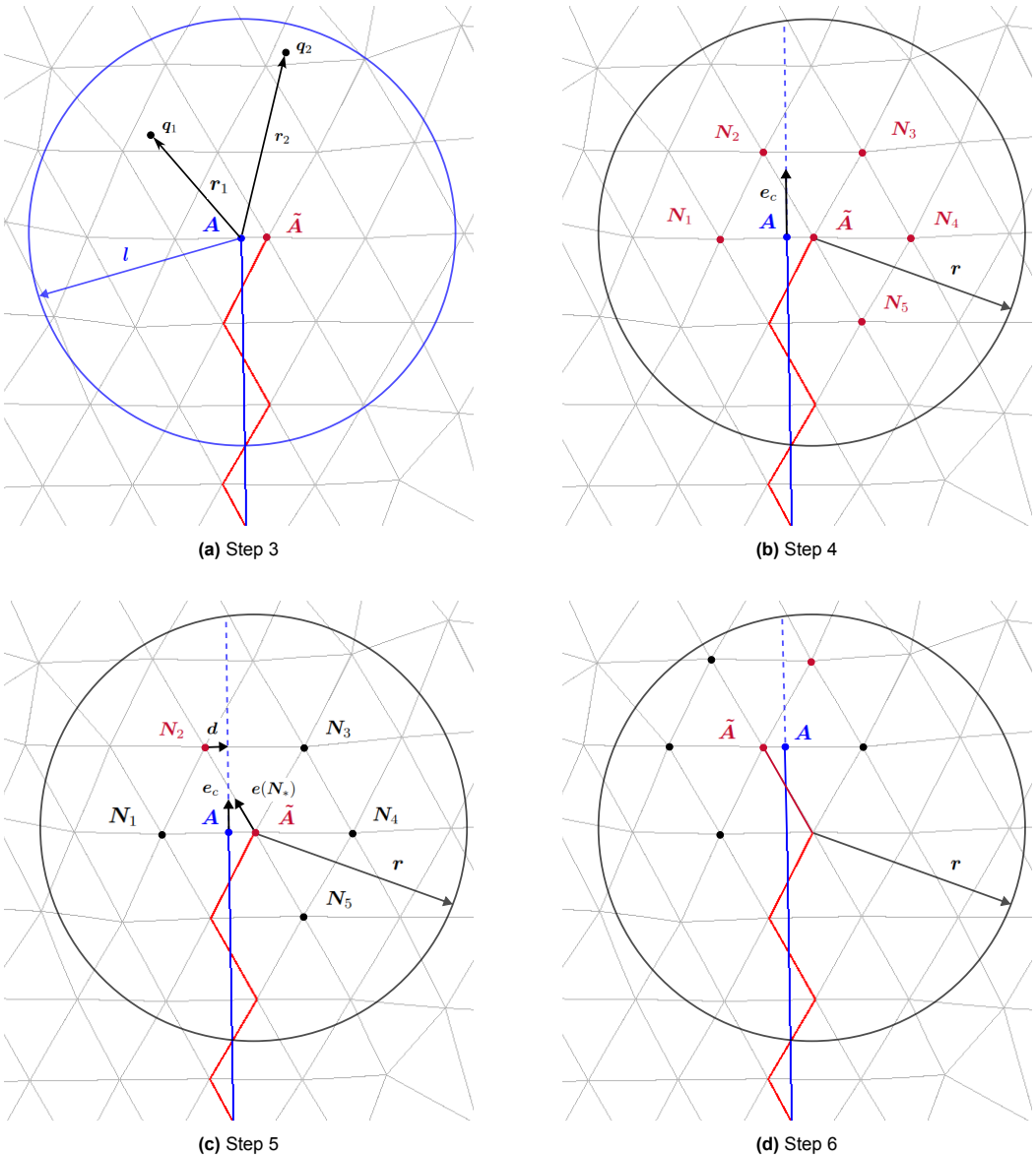

(a) Step 3 **(b)** Step 4

(c) Step 5 **(d)** Step 6

Figure 3.2: Visualization of the crack propagation strategy of a two-dimensional fracture. The approximated crack is plotted in blue, and the shifted (surrogate) crack path is plotted in red.

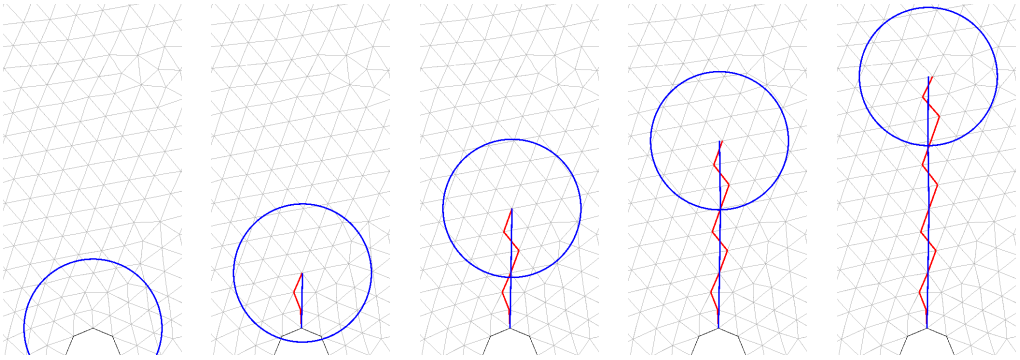

Figure 3.3: Crack path and crack propagation circle at different stages of the fracture propagation. The approximated crack is plotted in blue, and the shifted (surrogate) crack path is plotted in red for different loading stages.

In Section 3.1.2, it was identified that the `checkCommit_` function must be modified to integrate the new crack propagation algorithm. To achieve this:

- The new functions described in this section were implemented into `checkCommit_`.
- The previous Ortiz model functions responsible for crack propagation (`CheckFailure_` and `CheckFailureNStress_`) were removed.

3.1.4. Shifting of the cohesive zone conditions and weak form equations

The shifting of the cohesive zone conditions and weak form equations, based on Taylor expansions, was detailed in Section 2.4.2. This section focuses on the numerical implementation of these principles within the `getMatrixCoh_` function of the Ortiz model. This function assembles element stiffness matrices and force vectors for cohesive elements by computing cohesive tractions from the displacement jump and cohesive law, then updating the global stiffness matrix and force vector. To incorporate the shifted cohesive zone conditions and weak form equations, the following modifications and new functions were implemented:

Shifting the cohesive zone conditions (displacement jump)
The displacement jump is shifted via a first-order Taylor expansion (Equation 2.31). This process required the implementation of the following new functions:

- `getMapping_`
  - Computes closest distance from integration point of a cohesive element to the crack path.
  - Returns the closest distance and the normal vector of the crack path at the closest point. (Detailed calculations and visualization are provided in Section 2.4.2)
- `gradientJump_`
  - Assembles the displacement gradients of adjacent bulk elements at the integration point.
  - Computes the gradient of the displacement jump by subtracting the displacement gradients (see Figure 2.11).
- `taylorShift_`
  - Uses the distance from `getMapping_`, the computed gradient from `gradientJump_`, and the original displacement jump to apply the first-order Taylor expansion and compute the shifted displacement jump.

The cohesive zone model remains the same, and the shifted displacement jump is applied to the existing cohesive law for traction calculations. For details on the cohesive zone model, see Section 2.2. The SFM is designed to be compatible with any cohesive law. To maintain consistency with the Ortiz model, the shifted cohesive law is adopted (see Section 2.3.2). This choice ensures that cohesive forces are represented in a manner consistent with the existing framework, simplifying the implementation of the SFM into the finite element code.

Implementing shifted weak form equations
In Section 2.4.3, the differences between the weak form equations of the Ortiz model and the SFM were highlighted. The key differences include:

- The area correction term: $\boldsymbol{n} \cdot \tilde{\boldsymbol{n}}$
- Additional correction terms on the crack boundary, namely:
  - The stress jump term: $[\![\boldsymbol{\sigma}(\boldsymbol{u})]\!]\tilde{\boldsymbol{n}}$.
  - The mean stress term: $\{\!\{\boldsymbol{\sigma}(\boldsymbol{u})\}\!\}\tilde{\boldsymbol{n}}$.

To implement these additional crack boundary terms, their linearized discrete forms must first be derived. A detailed derivation of their contributions to the element force vector and tangent stiffness matrix is provided in Appendix A.

The area correction term is implemented into the linearized discrete formulation of the weak form equations, where the normal vectors are obtained as follows:

- $\tilde{n}$ (the normal vector of the surrogate edge) is obtained using `getNormals` (already implemented).
- n (the normal vector of the crack path) is computed using `getMapping_`.

As discussed in Section 2.4.3, this term is multiplied by the contributions associated with the crack boundary.

The additional correction terms, the stress jump and stress mean, are implemented by incorporating their respective element force vector contributions. However, during testing, the contributions to the tangent stiffness matrix did not perform as expected, likely due to an error in the derivation. Consequently, all SFM simulations were conducted using the force vector contributions of these terms while omitting their tangent stiffness contributions. Although this resulted in slightly slower convergence, the method remained functional. The functions described in this section were implemented into the `getMatixCoh_` function.

3.1.5. Partially implemented versions

To better understand the key components of the SFM, two partially implemented versions of the method are tested alongside the full implementation. This also helps evaluate the applicability and limitations of the method when applied to complex fracture scenarios and FRP composites.

From Section 2.1, it is shown that in the shifted weak form equations, the crack boundary terms are multiplied by an area correction term ($n \cdot \tilde{n}$). This term corrects the difference between the surrogate crack surfaces in the discrete mesh and the true crack surface in the continuum, ensuring that the effective crack surface area is accurately accounted for in the computations. The primary purpose of this correction term is to reduce mesh dependency. By applying the area correction term, the actual contribution of the cohesive forces along the crack is computed more accurately, regardless of the chosen mesh.

Since mesh dependency is a known issue in the Ortiz model, it is interesting to investigate how the area correction term affects the model's performance. To this end, two alternative versions are developed and tested alongside the full implementation:

- **Reduced SFM (Ortiz + Area + Propagation):** This version builds upon the Ortiz model by adding the area correction term and the crack propagation algorithm. However, it excludes the shifted interface conditions and the two additional correction terms in the shifted weak form equations. By leaving out the Taylor expansions and additional correction terms, this reduced implementation achieves lower computational complexity. The goal is to investigate the importance of the combination of the area correction term and the crack propagation algorithm in improving accuracy and reducing mesh dependency.
- **Extended Ortiz model (Ortiz + Area):** This version extends the Ortiz model by only adding the area correction term. The crack propagation algorithm, the shifted interface conditions, and the two additional correction terms in the shifted weak form equations are not included. The goal of this version is to evaluate whether the area correction term alone can improve mesh dependency and overall accuracy without the crack propagation algorithm. While the Ortiz model has been successful in predicting cracks in FRP composites, its results remain highly mesh-dependent. This version investigates whether mesh dependency can be reduced without significantly increasing the complexity of the original model.

Testing these two versions provides valuable insights into which components are critical for reducing mesh dependency and predicting accurate results.

3.1.6. Summary of the implementation

To conclude this section, Table 3.2 provides an overview of the new and modified functions implemented during the integration of the SFM into the Ortiz model. The table highlights each function's purpose and whether it was newly implemented or modified from the existing code. Additionally, Table 3.3 provides an overview of the different models used during the testing phase. The table outlines which key components of the SFM are included or excluded in each version, providing a clear overview of the tested configurations.

Table 3.2: Overview of implemented and modified functions.

Function	Purpose	Status
`checkCommit`	Modified to crack propagation algorithm of the SFM.	Modified
`checkCrackPropagation_`	Checks fail value of crack tips.	Newly implemented
`computeStressesInCircle_`	Calculates stresses and crack direction.	Newly implemented
`crackPropagation_`	Propagates the crack along the computed direction.	Newly implemented
`getClosestNodeToCrackTip_`	Identifies the closest node to the crack tip.	Newly implemented
`getMapping_`	Computes distance and normal vector from the surrogate to the crack.	Newly implemented
`getMatrixCoh_`	Added Taylor expansion, area correction terms, and correction terms.	Modified
`gradientJump_`	Computes the gradient of the displacement jump.	Newly implemented
`initializeCrackHistories_`	Initializes crack history and assigns crack IDs.	Newly implemented
`writeCrackPath_`	Outputs crack tips for postprocessing.	Newly implemented

Table 3.3: Overview of the tested models and their key components from the SFM.

Model	Area correction term	Crack propagation algorithm	Shifted interface conditions	Additional correction terms
Ortiz model	×	×	×	×
Extended Ortiz Model	✓	×	×	×
Reduced SFM	✓	✓	×	×
Full SFM	✓	✓	✓	✓

3.2. Challenges in applying the SFM to FRP composites

FRP composites are complex materials composed of densely packed fibers embedded in a polymer matrix. Both experimental studies and numerical simulations have frequently reported the phenomenon of densely distributed cracking, which ultimately coalesces into a single dominant crack [2, 12]. On the microscale, FRP composites are primarily characterized by matrix-fiber debonding and matrix cracking, as the fibers have significantly higher cohesive strength and typically remain intact. When analyzing a finite element mesh of an FRP composite (see Figure 3.4), it quickly becomes evident that the SFM cannot be directly applied without significant modifications. This section discusses the primary challenges associated with applying the SFM to FRP composites.

Challenges

1. **Cracks form in multiple, unpredictable locations** Cracks in composites can initiate in random locations, making them difficult to predict. However, the current SFM methodology works with predefined crack tips or multiple predefined crack tips from which cracks propagate. This presents a significant limitation for composites, as new cracks cannot spontaneously emerge during a simulation. To address this issue, the method should be capable of initiating cracks based on stress control across the entire domain. With such a dynamic approach, it would become possible to better model the distributed cracking behavior of composites.
2. **Crack propagation into fibers** In the current implementation of the SFM, the crack direction is determined by the maximum principal tensile stress. When a crack tip reaches the cohesive strength, the crack propagates a predefined distance in that direction. However, if the crack tip enters a fiber, the higher cohesive strength of the fiber prevents further crack growth. This would lead to inaccurate and unrealistic results in the simulation. A possible solution would be to halt propagation once a crack reaches the boundary of a fiber, ensuring that cracks remain within the matrix.
3. **Crack propagation along fiber boundaries** When a crack tip reaches the edge of a fiber, the crack should propagate along the curved surface of the fiber rather than simply following the direction of maximum principal tensile stress. This requires a new algorithm to account for such situations. The current SFM does not support this functionality, even though it is crucial for accurately modeling matrix-fiber debonding, a typical phenomenon in composites.
4. **Cracks along curved paths** Matrix-fiber debonding often partially follows the curved edges of fibers, as the cohesive strength at the matrix-fiber interface is lower than within the matrix itself. Accurately simulating this process poses a challenge, as the current SFM does not support curved crack paths. Although small incremental steps may provide a workaround, a more robust approach would involve developing a new algorithm that allows for the tracking of curved or circular paths.
5. **Formation of a dominant crack** In composites, it is common for multiple cracks to merge and evolve into a single dominant crack. To realistically simulate this process, mechanisms are required that allow for the merging and branching of cracks. Without such functionalities, the SFM cannot accurately represent the natural progression of a dominant crack.
6. **Cracks that close or become inactive** In certain cases, cracks may close or become inactive, for example, when they merge with other cracks or reach a boundary. The current implementation of the SFM does not account for such scenarios. Modifications are needed to ensure that closed or inactive cracks are properly tracked and deactivated.

The challenges outlined above highlight the need for significant improvements to make the SFM suitable for application to FRP composites. The following section will explain how the challenges related to crack initiation, as well as crack merging and termination at boundaries, are addressed, as these aspects are essential for successfully modeling composite behavior.

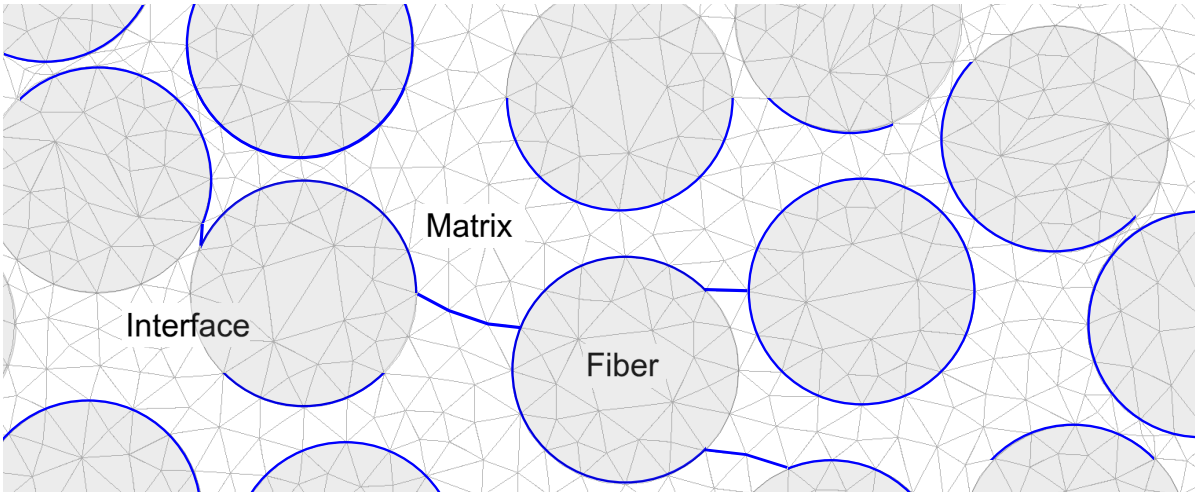

Figure 3.4: Snapshot of the finite element mesh of a fiber-reinforced polymer (FRP) composite with the observed crack distribution. The fibers are shown in grey, the matrix in white, and the crack distribution in blue.

3.3. Implementation of additional features

To address the challenges encountered in modeling FRP composites, this section focuses on the implementation of two key features. The first is crack initialization, which enables the method to initiate cracks dynamically based on stress control across the entire domain. The second is crack merging and termination at boundaries, which ensures that multiple cracks can either combine into a single dominant crack or terminate naturally upon reaching the edges of the domain. These additional features have been implemented by modifying the crack propagation algorithm of the SFM. Elements from the Ortiz model, along with newly developed features, have been incorporated to accurately predict the unique behavior of composites.

3.3.1. Stress-based crack initialization

Crack initialization plays a critical role in accurately simulating the densely distributed cracking observed in FRP composites. In the Ortiz model, crack initiation is determined by a stress-based failure criterion, implemented through the `CheckFailure_` and `CheckFailureNstress_` functions. These functions evaluate the middle nodes of triangular elements for cohesive strength failure, allowing cracks to initiate at appropriate locations across the domain. While the original SFM crack propagation algorithm (see Section 3.1.3) included predefined crack initialization. However, this approach is insufficient for FRP composites, where cracks emerge dynamically throughout the material. To address this limitation, a stress-based approach was implemented, following these steps:

1. The `CheckFailure_` and `CheckFailureNstress_` functions were reintroduced into the `checkCommit` function, ensuring that failure criteria are evaluated before crack propagation occurs.
2. When failure is detected at a middle node, this location is stored as a crack tip and passed to the `initializeCrackHistories_` function.
3. A new crack branch is created and tracked in the `CrackHistory` class, allowing the crack to propagate in the correct direction using the existing propagation functions in `checkCommit`.

These modifications enabled dynamic crack initialization throughout the domain, ensuring that SFM accurately captures the distributed cracking behavior characteristic of FRP composites.

3.3.2. Crack merging and termination at boundaries

Crack merging and crack termination at boundaries are essential processes for accurately simulating the behavior of FRP composites. Crack merging focuses on the coalescence of multiple cracks into a single dominant crack path, a phenomenon commonly observed in FRP composites. On the other hand, crack termination at boundaries addresses the scenario where a crack ends upon reaching the edge of the domain. Both processes were implemented by modifying step 5 of the crack propagation algorithm, where surrogate edges are selected (see Section 3.1.3).

To incorporate these processes, the following criteria were introduced after identifying the set of nodes connected to the current surrogate crack tip:

1. **Crack termination at boundaries:** The node lies on the boundary of the mesh (see Figure 3.5b).
2. **Crack merging:** The node is part of another crack branch (see Figure 3.6b).

if either of these conditions is met, the node is designated as the endpoint of the crack, and the crack is extended to this location. For boundary termination, this behavior is illustrated in Figure 3.5. For merging, the crack merges with an adjacent branch, as shown in Figure 3.6. Once the process is complete, the current crack branch is marked as inactive and stored in an `inactiveCrackHistory` list within the `CrackHistory` class, preventing further propagation of the terminated or merged branch.

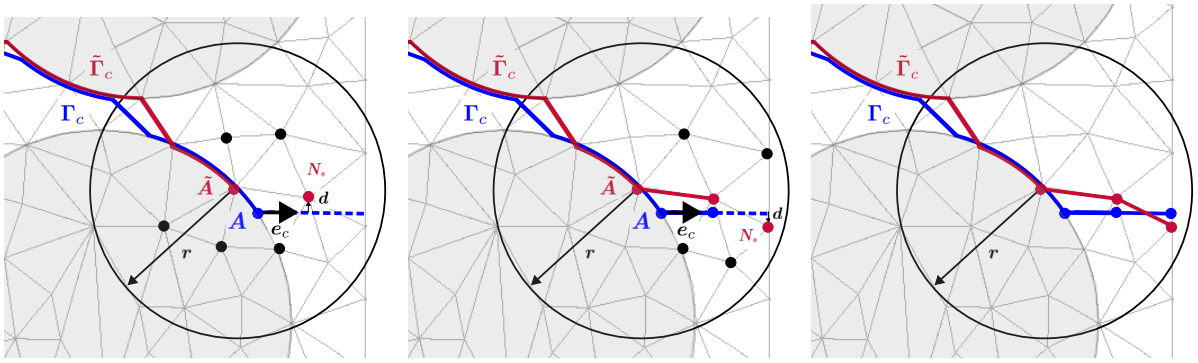

Figure 3.5: Crack termination at the boundary of the mesh.

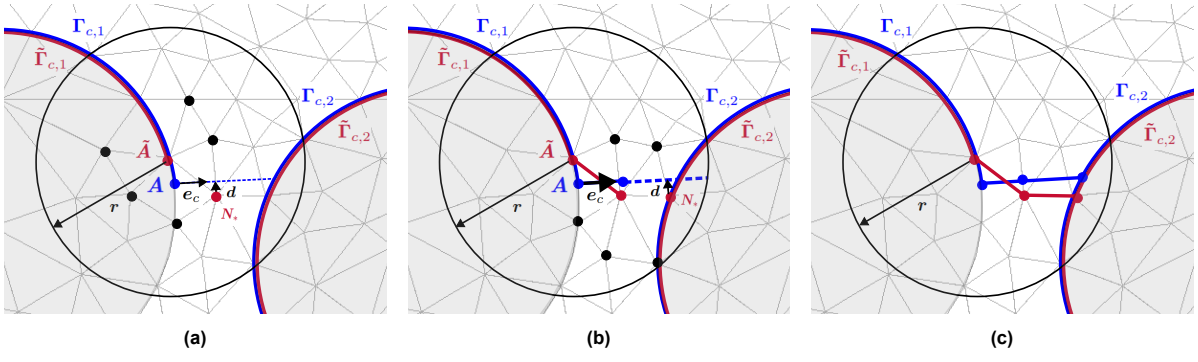

Figure 3.6: Crack merging with another crack branch.

4

Results

This chapter presents the results of a series of numerical simulations performed to evaluate the performance of the newly proposed shifted fracture method (SFM) in comparison to the Ortiz model. Alongside the full implementation of the SFM, two alternative versions are evaluated, the reduced SFM (Ortiz + Area + Propagation) and the extended Ortiz model (Ortiz + Area). All simulations are performed in two dimensions under the plane strain assumption, with the primary focus on the accuracy of crack path prediction in both simple and complex geometries.

Section 4.1 presents a verification and validation study comparing the full SFM implementation and the reduced SFM against the Ortiz model. Where applicable, the results are also compared to those presented in the original SFM paper [15]. Section 4.2 examines the extended Ortiz Model separately, focusing on how the area correction term alone impacts accuracy and mesh dependency. Finally, Section 4.3 investigates the effectiveness of the implemented additional features in addressing specific challenges related to crack path prediction in fiber-reinforced polymer (FRP) composites.

4.1. Verification and validation of the SFM

This section presents a verification and validation study of the full SFM and the reduced SFM implementation, as described in Section 3.1.5. Three numerical tests are conducted to assess the methods' ability to predict crack paths, comparing their results with those of the Ortiz model and, where applicable, benchmarks from the original SFM publication.

In the numerical experiments, three different test configurations are considered: a compact tension (CT) test that involves crack propagation along a straight crack path; an L-shape panel test, where the crack follows a curved crack path in a complex geometry; and a four-point bending test (FPBT), which also examines a curved crack path but in a more moderately complex geometry. Since the CT test is not included in the original SFM publication, its results are compared exclusively with those of the Ortiz model. For both the L-shape panel test and the FPBT, results are also compared with those reported in the original SFM paper.

Key evaluation metrics include load-displacement curves, mesh size dependence, and the convergence of dissipated energy. These metrics provide a comprehensive assessment of SFM's accuracy, reliability, and robustness in predicting crack paths across a range of scenarios.

4.1.1. Compact tension (CT) test

The geometry of the CT specimen is shown in Figure 4.1. It consists of a rectangular beam with a height of $b = 30$ mm, a length of $l = 50$ mm, and a centrally located notch on the bottom edge with a height of $bn = 10$ mm and a width of $ln = 2$ mm. The material properties are defined as follows: Young's modulus $E = 40$ GPa, Poisson's ratio $\nu = 0.2$, normal critical stress $t_{cr} = 20$ MPa, and fracture energy $G_F = 200$ N/m. The specimen is simply supported along its bottom edge. To prevent rigid body rotation, constraints are applied in the x-direction at both the bottom-left and bottom-right corners. A displacement $\boldsymbol{u}$ is imposed on the second half of the bottom edge, as illustrated in Figure 4.1.

Four computational grids (denoted as Mesh 1, Mesh 2, Mesh 3, and Mesh 4) were used in the numerical simulations, as summarized in Table 4.1. The average mesh sizes near the crack path were $\boldsymbol{h} = 2$ mm, $\boldsymbol{h} = 1$ mm, $\boldsymbol{h} = 0.5$ mm, and $\boldsymbol{h} = 0.25$ mm, respectively. To enhance computational efficiency, the mesh was coarsened in regions further from the crack path.

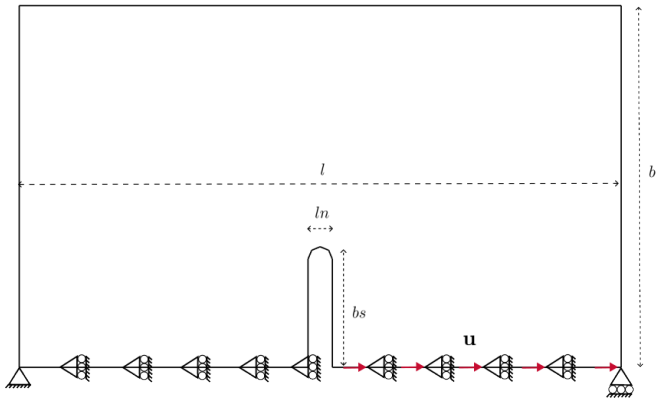

Figure 4.1: Geometry and setup of the CT specimen.

Table 4.1: Mesh properties for the CT specimen.

Meshes	Number of DOFs	Element size h
Mesh 1	5,908	2.0 mm
Mesh 2	8,810	1.0 mm
Mesh 3	19,150	0.5 mm
Mesh 4	33,196	0.25 mm

As the displacement u increases, the top of the notch is the first location where the principal stress reaches the normal critical stress t_{cr}, initiating crack propagation along a vertical path. Since the crack path is known in advance, the true load-displacement curve can be determined using the Ortiz model by aligning element edges along the predefined vertical crack path. This load-displacement curve serves as a reference for evaluating the accuracy of other methods.

Figure 4.2 compares the crack paths computed using the full SFM (magenta line), reduced SFM (blue line), the Ortiz model (green line), and the reference solution (black dotted line) for all four mesh configurations. Figures 4.3a, 4.3b, 4.3c, and 4.3d present the load-displacement curves for the reference solution, the full SFM, reduced SFM, and the Ortiz model across all mesh sizes. The same color scheme is used for the load-displacement curves as for the crack paths, as indicated in the legend.

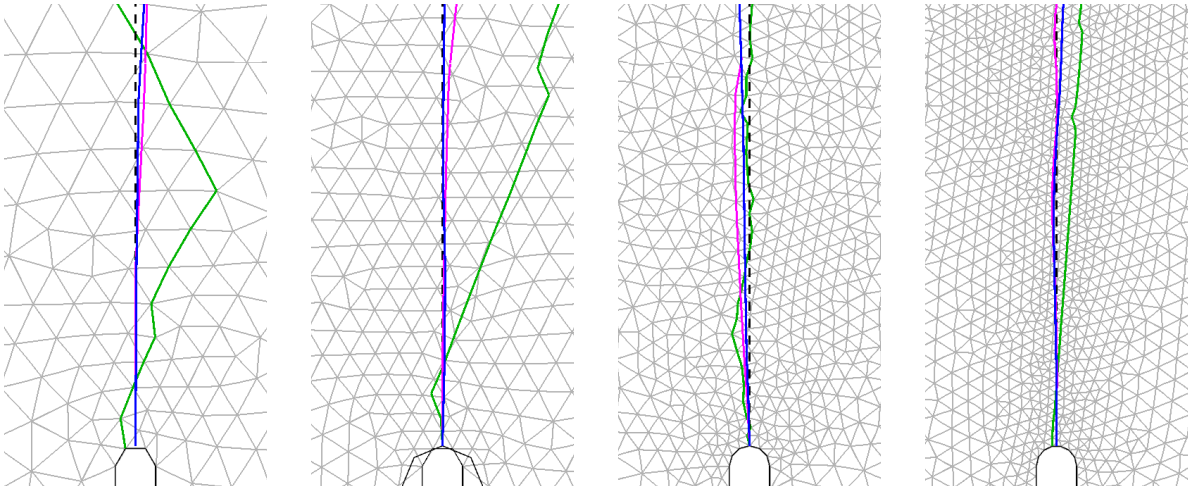

Figure 4.2: Comparison of crack paths across four meshes for the full SFM (magenta line), reduced SFM (blue line), the Ortiz model (green line), and the reference solution (black dotted line).

As shown in Figure 4.2, the Ortiz model exhibits strong mesh dependence, where the predicted crack paths are constrained by the finite element mesh and can only propagate along element edges. For coarser meshes, significant deviations from the reference crack path are observed. As the mesh is refined, the crack paths gradually converge toward the vertical reference crack path. In contrast, both the full SFM and the reduced SFM implementation accurately predict the reference crack path, even for the coarsest mesh, and the crack path remains consistent as the mesh is further refined.

Figures 4.3a through 4.3d present the load-displacement curves, which exhibit a ductile material response. The Ortiz model demonstrates clear mesh dependency; for the coarsest mesh (Mesh 1), the peak load is approximately 10 N higher than that of the reference solution. As the mesh is refined, this difference decreases, and for the finest mesh (Mesh 4), the peak load matches the reference solution, indicating improved accuracy with finer mesh sizes. Both the full SFM and reduced SFM implementations produce load-displacement curves that closely follow the reference solution, even for the coarsest mesh. Unlike the Ortiz model, the SFM methods do not exhibit significant mesh dependency, as the results remain consistent across all mesh sizes.

In the Ortiz model and the reduced SFM, sharp unloading effects are observed in the coarser meshes (Meshes 1 and 2) when a new cohesive element is inserted. This effect diminishes as the mesh is refined and is no longer visible in finer meshes (Meshes 3 and 4). For the full SFM implementation, a different behavior is observed: instead of unloading, the equilibrium path exhibits sudden vertical drops. Similar to the unloading effects, these vertical drops disappear as the mesh is refined.

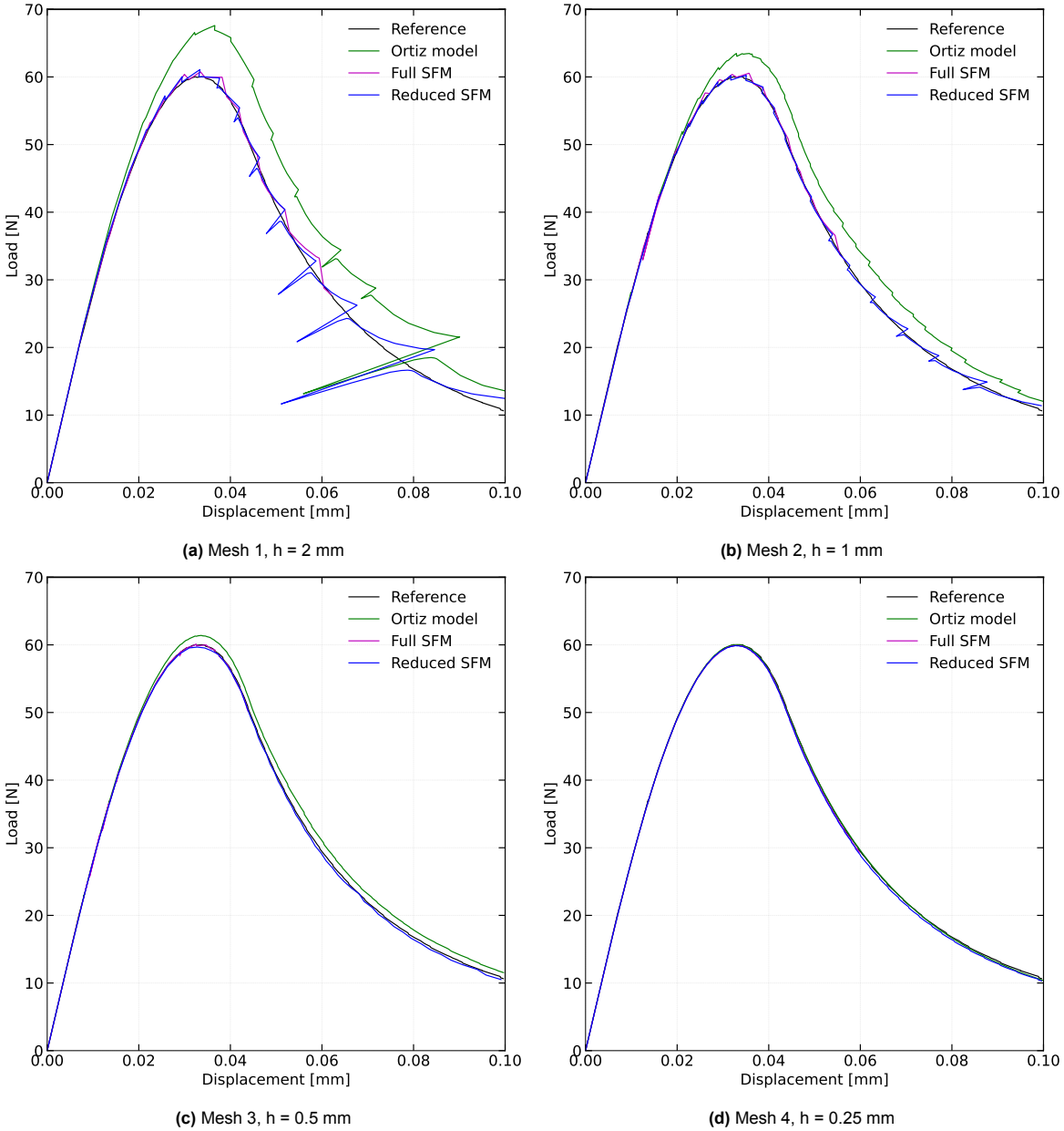

(a) Mesh 1, h = 2 mm

(b) Mesh 2, h = 1 mm

(c) Mesh 3, h = 0.5 mm

(d) Mesh 4, h = 0.25 mm

Figure 4.3: Load-displacement curves for the full SFM (magenta line), reduced SFM (blue line), the Ortiz model (green line), and the reference solution (black line)

Figure 4.4 presents the dissipated energy error ε for the CT test, comparing the reduced SFM (blue curve) and the Ortiz model (green curve). The error is computed for each mesh as follows:

$$\varepsilon = \frac{|E_{\text{reference}} - E_i|}{E_{\text{reference}}} \tag{4.1}$$

where ε represents the dissipated energy error, E_i denotes the total dissipated energy for a given mesh, and $E_{\text{reference}}$ corresponds to the total dissipated energy obtained from the reference solution. The error is plotted as a function of the total number of degrees of freedom (DOFs) to illustrate the convergence behavior. The results show that the Ortiz model converges at a first-order rate with respect to the dissipated energy error. In contrast, the reduced SFM achieves significantly faster convergence, demonstrating quadratic or higher-order accuracy as the mesh is refined.

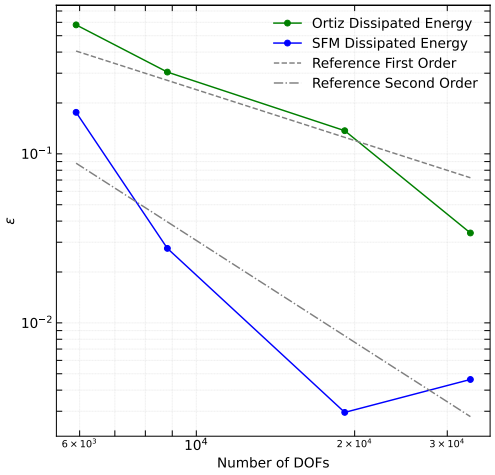

Figure 4.4: Dissipated fracture energy ε for the CT test, comparing the reduced SFM (blue curve) and the Ortiz model (green curve).

In the next sections and subsections, the reduced SFM will be used instead of the full SFM implementation. This decision is based on the observation that the reduced SFM, which includes only the crack propagation algorithm and the area correction term, produced highly accurate results in the CT test. While the full SFM implementation also achieved highly accurate results, the tangent stiffness matrix contributions in this implementation did not perform as expected. Consequently, these contributions were omitted from the final implementation, which, in turn, resulted in slower convergence. Given the slower convergence of the full implementation and the strong performance of the reduced SFM, the latter was chosen for further testing.

4.1.2. L-shape panel test

To further verify and validate the reduced SFM, a numerical example involving a curved crack path is analyzed using an L-shape panel test. The geometry of the L-shape panel specimen is shown in Figure 4.5, with dimensions $\boldsymbol{a} = 250$ mm, $\boldsymbol{b} = 220$ mm, and a thickness of $\boldsymbol{t} = 10$ mm. The material properties are defined as follows: Young's modulus $\boldsymbol{E} = 20$ GPa, Poisson's ratio $\boldsymbol{\nu} = 0.18$, fracture energy $\boldsymbol{G}_F = 100$ N/m, normal critical stress $\boldsymbol{t}_{cr} = 20$ MPa, and shear effect parameter $\boldsymbol{\beta} = 1.5$. Two computational grids (denoted as Mesh 1 and Mesh 2) are used in the numerical simulations, as summarized in Table 4.2.

This numerical example has been widely studied in the literature, both experimentally and numerically. Previous studies include investigations using the SFM [15, 16], XFEM numerical results [24, 25], and experimental findings by Winkler [26].

Figure 4.6 presents the computed crack paths and load-displacement curves for the L-shape panel test, comparing the reduced SFM implementation (blue) and the Ortiz model (green) across both mesh sizes. Additionally, the figure includes the SFM results from Li et al. [16] (red), which use the stress intensity factor (SIF) criterion for selecting the crack propagation direction, and the experimental results

from Winkler, represented by uncertainty brackets as a gray shaded area. For the reduced SFM implementation, the maximum principal tensile stress criterion was used to determine the crack propagation direction.

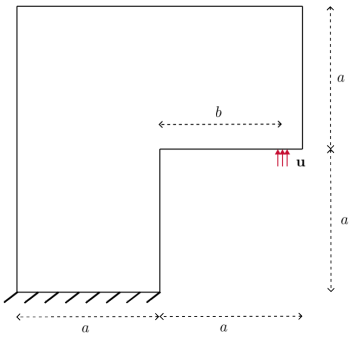

Figure 4.5: Geometry and setup of the L-shape panel specimen.

Table 4.2: Mesh properties for L-shape panel specimen.

Meshes	Number of DOFs	Element size h
Mesh 1	22,578	5.0 mm
Mesh 2	41,030	2.5 mm

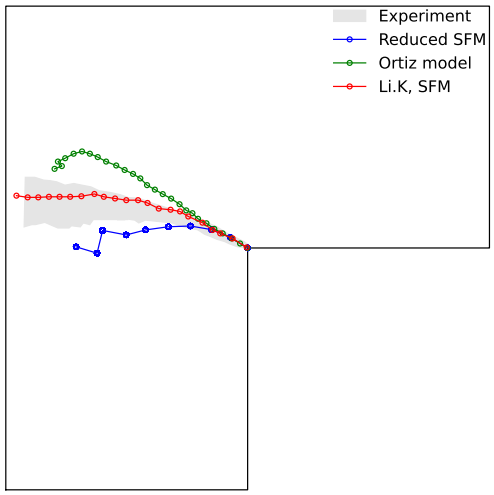

(a) Crack paths, mesh 1

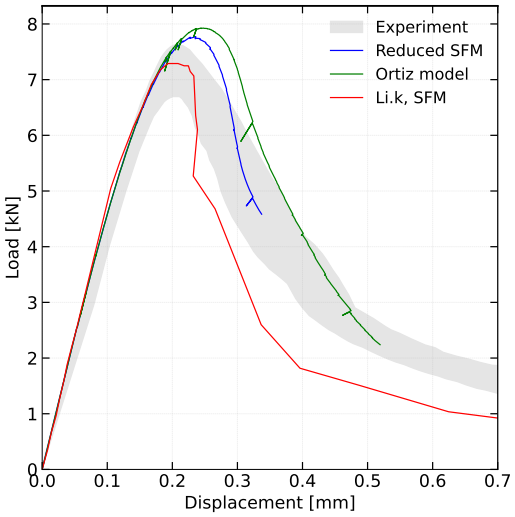

(b) Load-displacement curves, mesh 1

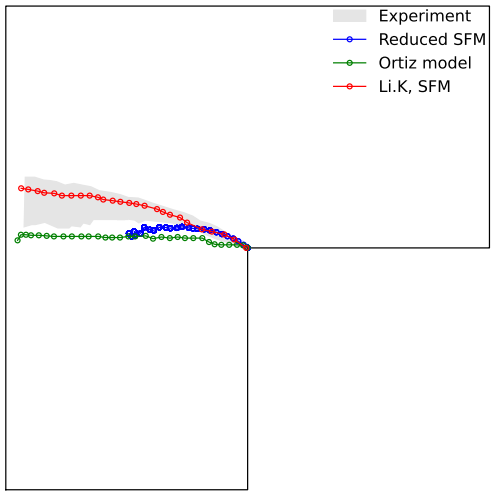

(c) Crack paths, mesh 2

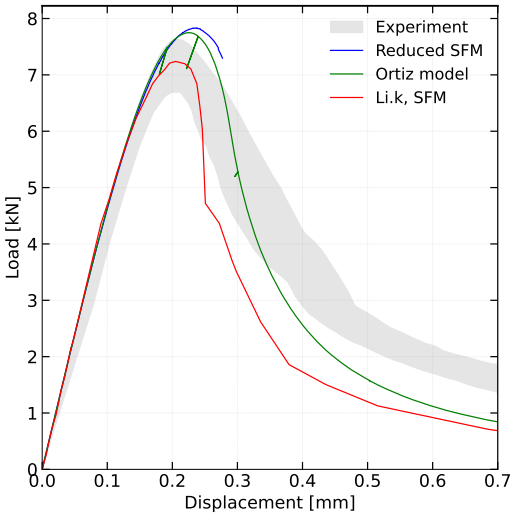

(d) Load-displacement curves, mesh 2

Figure 4.6: Comparison of crack paths and load-displacement curves for the reduced SFM implementation (blue curves), the Ortiz model (green curves), the SFM results from Li et al. (red curves), and the experimental results from Winkler (gray shaded area) across two different mesh sizes.

Figure 4.7 presents the crack paths and load-displacement curves of the reduced SFM implementation, comparing its results for both mesh sizes with the XFEM simulations by Dumstorff and Meschke [24], which also applied the maximum principal tensile stress criterion. The experimental results from Winkler are again included as a reference, represented by the gray shaded area.

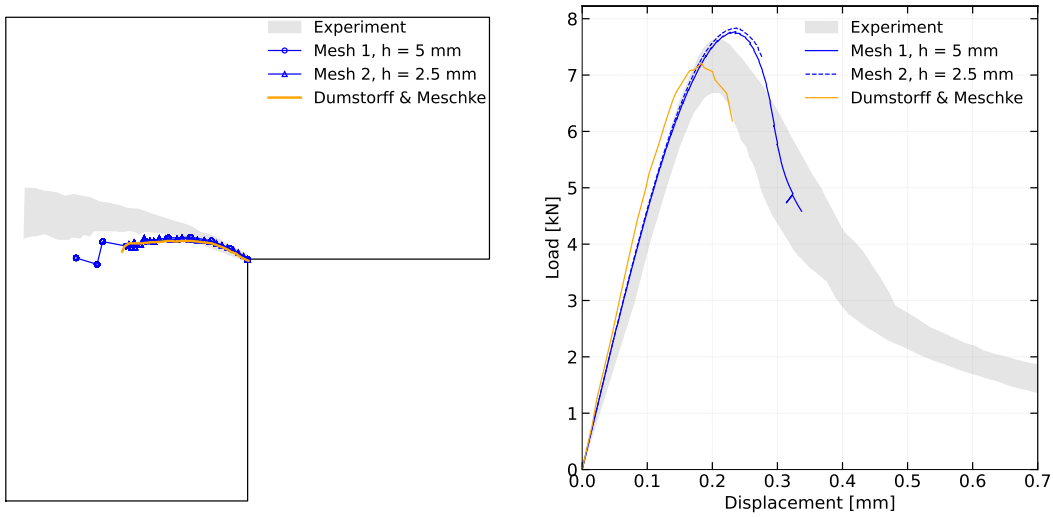

(a) Comparison of crack paths

(b) Comparison of load-displacement curves

Figure 4.7: Comparison of crack paths and load-displacement curves for the reduced SFM implementation (blue curves) across two different mesh sizes, the XFEM simulations by Dumstorff and Meschke [24] (orange curves), and the experimental results from Winkler [26] (gray shaded area)

Figures 4.6a and 4.6c illustrate that the Ortiz model initially follows a crack path similar to that reported in the SFM papers 4.7a. However, as the crack propagates, significant deviations occur. The finer mesh provides a closer approximation but still deviates considerably from the results presented in the SFM paper and does not fall within the experimental uncertainty bracket of the experiments conducted by Winkler. A similar trend is observed for the reduced SFM, where both mesh sizes initially follow a crack path comparable to the results in the SFM paper. However, at approximately halfway along the crack path, convergence issues arise, ultimately causing the simulation to terminate prematurely. In contrast, the results in the SFM papers, where crack propagation was determined using the stress intensity factor (SIF) criterion, do not exhibit these issues. The crack path in their study remains stable throughout the simulation, aligns well with reference results, and falls within the experimental uncertainty bracket of Winkler's experiments.

Figures 4.6b and 4.6d show that the Ortiz model exhibits mesh dependency in the load-displacement curves. The coarser mesh produces a higher peak load than the reference results, while the finer mesh provides a closer match. For the reduced SFM model, the load-displacement curves for both mesh sizes are nearly identical. However, the curves terminate shortly after reaching the peak load.

Figure 4.7 shows that the results of the reduced SFM model for both mesh sizes align with the findings reported by Dumstorff and Meschke [24], where the same criterion, the maximum principal tensile stress, was used to determine the crack propagation direction. Their study found that the computed crack path deviated significantly from the experimental range, with a sharp deviation occurring shortly after the peak load was reached. Following this deviation, the numerical results were no longer considered reliable. This closely matches the behavior observed in the reduced SFM results.

4.1.3. Four-point bending test (FPBT)

Finally, an FPBT is performed to further assess the SFM's ability to predict curved crack propagation. Figure 4.8 illustrates the geometry and setup of the test. The specimen has the following geometrical properties: height $b = 200$ mm, length $l = 800$ mm, $a = 80$, and a centrally located notch on the top edge with length $ln = 40$ mm. The material properties are defined as follows: Young's modulus $E = 28$ GPa, Poisson's ratio $\nu = 0.1$, normal critical stress $t_{cr} = 1.75$ MPa, and fracture energy $G_F = 100$ N/m. The specimen is supported at two locations and is loaded by two forces, F_1 and F_2, which are

distributed over a strip of length 20 mm, as depicted in Figure 4.8. A single computational grid is used in the numerical simulations, with an average mesh size $\boldsymbol{h} = 5$ mm in the region surrounding the crack path.

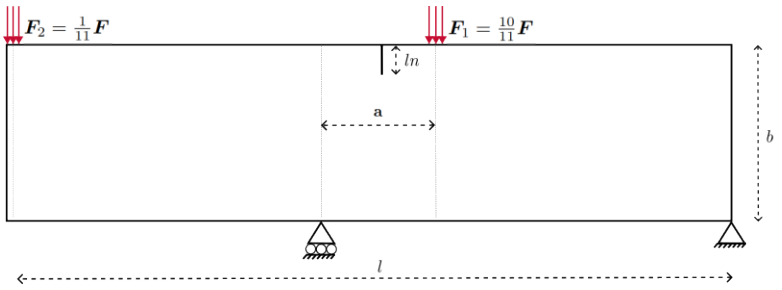

Figure 4.8: Geometry and setup of the four-point bending specimen test.

The four-point bending test has been extensively studied in the literature, both experimentally and numerically. Previous research includes investigations using the SFM method [15, 16], XFEM numerical simulations [27], and experimental findings reported in [28].

Figures 4.9a and 4.9b present a comparison of the computed crack paths and load-displacement curves, respectively, for the FPBT. The crack paths in Figure 4.9a include results from the reduced SFM implementation (blue), the SFM results by Li et al. [15] (red), and the experimental results reported by [28] (black). Figure 4.9b shows the load-displacement curves, illustrating both F_1 and F_2 as defined in the experimental setup. The reduced SFM is again compared to the results from Li et al. and the experimental data.

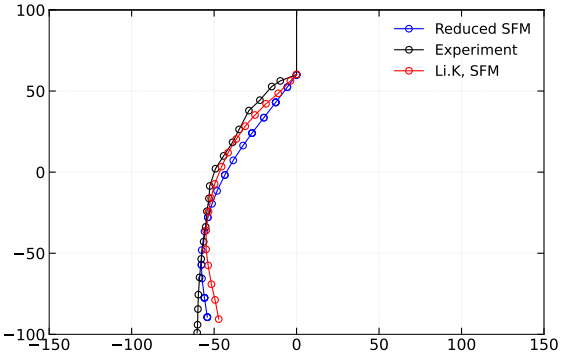

(a) Comparison of crack paths

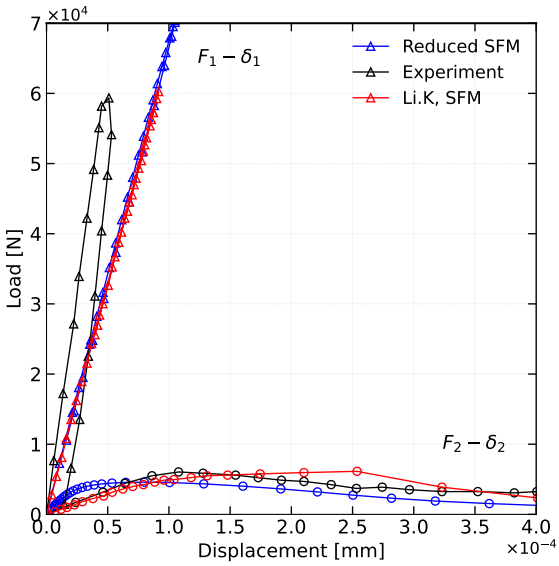

(b) Comparison of load-displacement curves

Figure 4.9: Comparison of crack paths and load-displacement curves for the four-point bending test (FPBT), including results from the reduced SFM (blue), the SFM by Li et al. [15] (red), and the experimental results [28] (black).

From Figure 4.9, it can be observed that both the crack path and the load-displacement curve predicted by the reduced SFM closely align with the numerical results reported in the SFM paper and the experimental results. In Figure 4.9b, the most notable observation is the occurrence of very severe snap-back behavior under the load $\boldsymbol{F}_1$, which is also evident in the results presented in the SFM paper. Additionally, an attempt was made to test the Ortiz model. However, the simulations failed to converge in every instance. Consequently, no results could be generated for the Ortiz model in this study.

4.2. Results of the extended Ortiz model

This section evaluates the performance of the extended Ortiz model developed to further simplify the SFM approach and evaluate whether the area correction term alone can improve mesh dependency by excluding all other key components of the SFM. The extended Ortiz model retains only the area correction term from the original SFM, combined with key elements of the Ortiz model, to reduce complexity while aiming for effective crack path prediction (see Section 3.1.5). This version specifically investigates whether mesh dependency can be reduced without significantly increasing the complexity of the Ortiz model.

To assess the extended Ortiz model, the CT test is considered, where the expected crack path follows a straight line. Two mesh configurations are considered: mesh 1 (h = 2 mm) and mesh 3 (h = 0.5 mm). The geometrical and material properties are described in Section 4.1.1.

Figure 4.10 presents the crack paths and load-displacement curves for both meshes. The results include the extended Ortiz model (blue), the Ortiz model (green), and the reference solution (black) for both the crack paths and load-displacement curves.

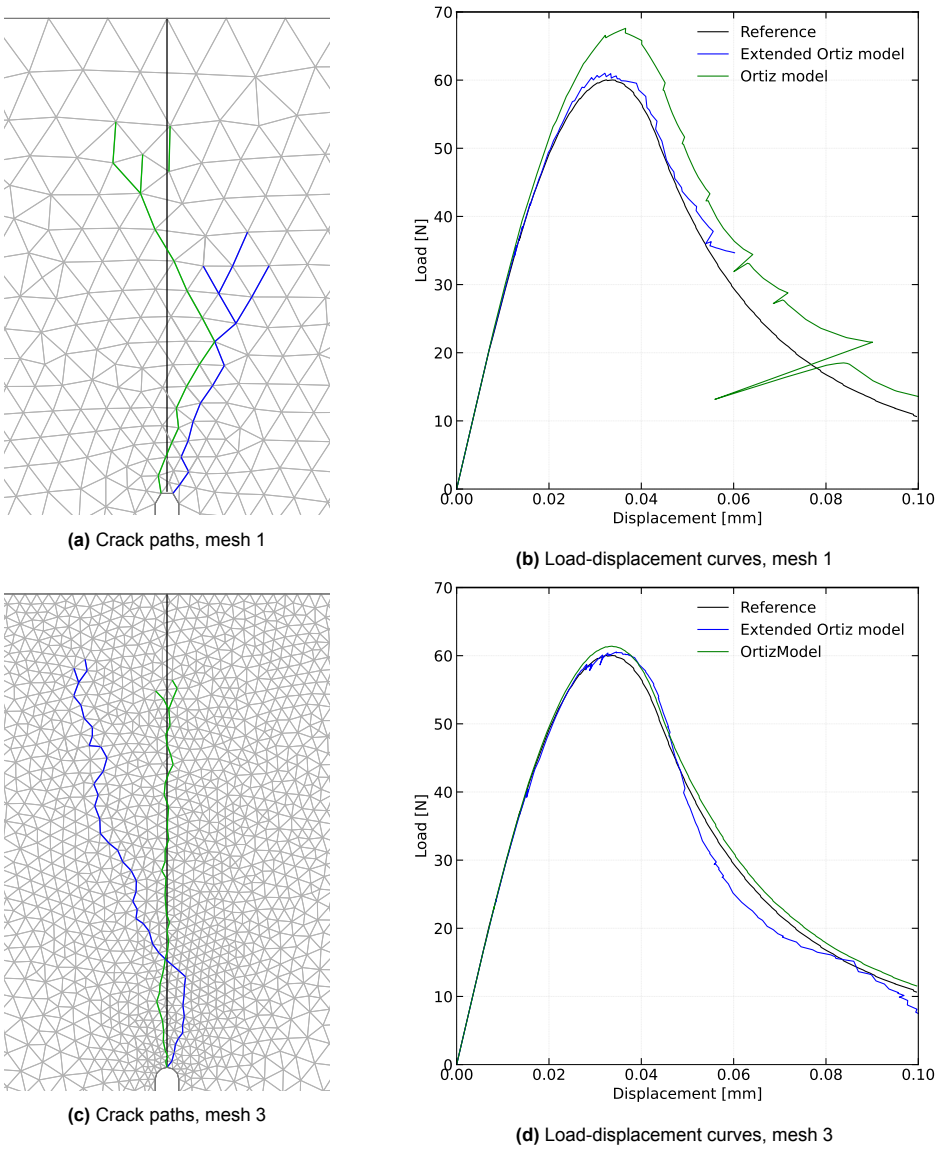

(a) Crack paths, mesh 1

(b) Load-displacement curves, mesh 1

(c) Crack paths, mesh 3

(d) Load-displacement curves, mesh 3

Figure 4.10: Comparison of crack paths and load-displacement curves for the CT test. The left column shows the crack paths and the right column shows the load-displacement curves. The top row represents the results for mesh 1, and the bottom row represents mesh 3. The models include the extended Ortiz model (blue), the Ortiz model (green), and the reference solution (black).

Figures 4.10a and 4.10c, which depict the crack paths for both mesh sizes, clearly show that the extended Ortiz model significantly deviates from the reference crack path. The figures also include the crack paths from the Ortiz model. For the coarser mesh, the results of the Ortiz model and the simplified model are approximately similar. However, for a finer mesh, the Ortiz model provides significantly better results, while the extended Ortiz model continues to show considerable deviations, even in a refined mesh.

Figures 4.10b and 4.10d illustrate the load-displacement curves for the extended Ortiz model. While the curves do not exhibit extreme deviations from the reference solution, they do not follow the reference trend as closely as observed in the full SFM and reduced SFM implementations. The Ortiz model is also included for comparison, demonstrating clear mesh dependency. Additionally, for mesh 1, the extended Ortiz model terminates prematurely due to convergence issues.

4.3. Results of additional features

This section evaluates the additional features implemented in the reduced SFM, including stress-based initialization, crack merging, and crack termination at boundaries, as described in Section 3.3. These features are tested using two simple test cases to validate their functionality and explore their potential for enhancing the robustness of the SFM in future applications. The first test case is the compact tension (CT) test, which was previously introduced and tested in Section 4.1.1. The second test case is the double-edge notched tension (DENT) test, which introduces a more complex scenario involving interacting cracks. By comparing the results with known crack path behavior, this section demonstrates the potential of these features to address specific challenges in crack path prediction and lay the groundwork for their application to more complex materials, such as FRP composites.

CT test

The features are tested using the CT test. For the geometrical and material properties, see Section 4.1.1. In this test, only mesh 1 is used, with an average element size around the crack path of h = 2 mm. Figure 4.11 shows the results of the crack path of the reduced SFM with the implemented features. The crack is shown in blue, the surrogate crack in red, and the reference solution in black.

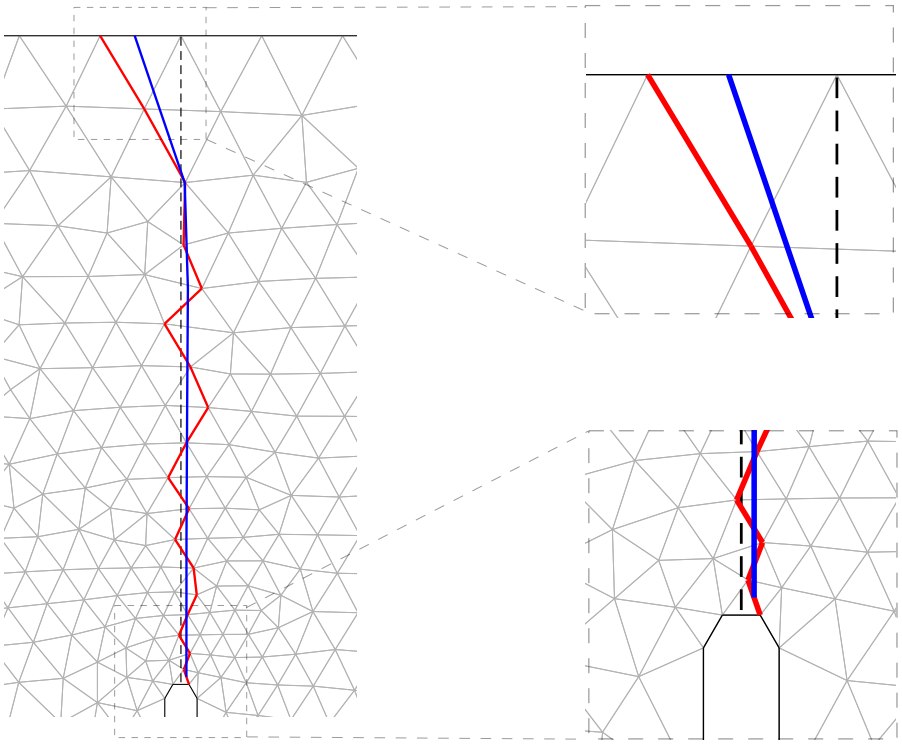

Figure 4.11: Results of the CT test for the reduced SFM with the implemented features. On the left, the crack (blue curve) and the surrogate crack (red curve) path are shown, while the right-side images present two zoomed-in views. The top-right image illustrates crack merging at the boundary of the mesh, while the bottom-right image highlights crack initiation.

From the left side of Figure 4.11, it can be seen that the crack path closely follows the reference solution, consistent with the results obtained without the additional features. On the right side of Figure 4.11, two zoomed-in areas from the left-side figure highlight the newly implemented features. The top-right zoomed view illustrates that when the crack reaches the boundary of the mesh, both the crack and surrogate crack are halted, demonstrating the implementation of crack termination at boundaries and preventing further propagation. The bottom-right zoomed view highlights the crack initiation process. Instead of predefining crack tips, the cracks are initialized based on the method originally used in the Ortiz model, where all the mid-nodes of six-noded triangular elements are checked. This figure demonstrates that the crack starts propagating from a middle node, though not exactly at the theoretical starting point of the crack.

DENT test

The second test is a DENT test. The geometry and boundary conditions are illustrated in Figure 4.12 (left). The specimen has the following geometrical properties: height $b = 150$ mm, length $l = 50$ mm, and a notch length of $l_n = 1$ mm for both centrally located notches. The material properties are defined as follows: Young's modulus $E = 40$ GPa, Poisson's ratio $\nu = 0.2$, normal critical stress $t_{cr} = 20.0$ MPa, and fracture energy $G_F = 200$ N/m. The specimen is supported at the bottom edge in both the x- and y-directions and is loaded on the top edge.

Figure 4.12 (middle) shows the crack (blue) and surrogate crack (red) paths for the reduced SFM. Additionally, Figure 4.12 (right) illustrates the crack paths at different loading stages of the simulation.

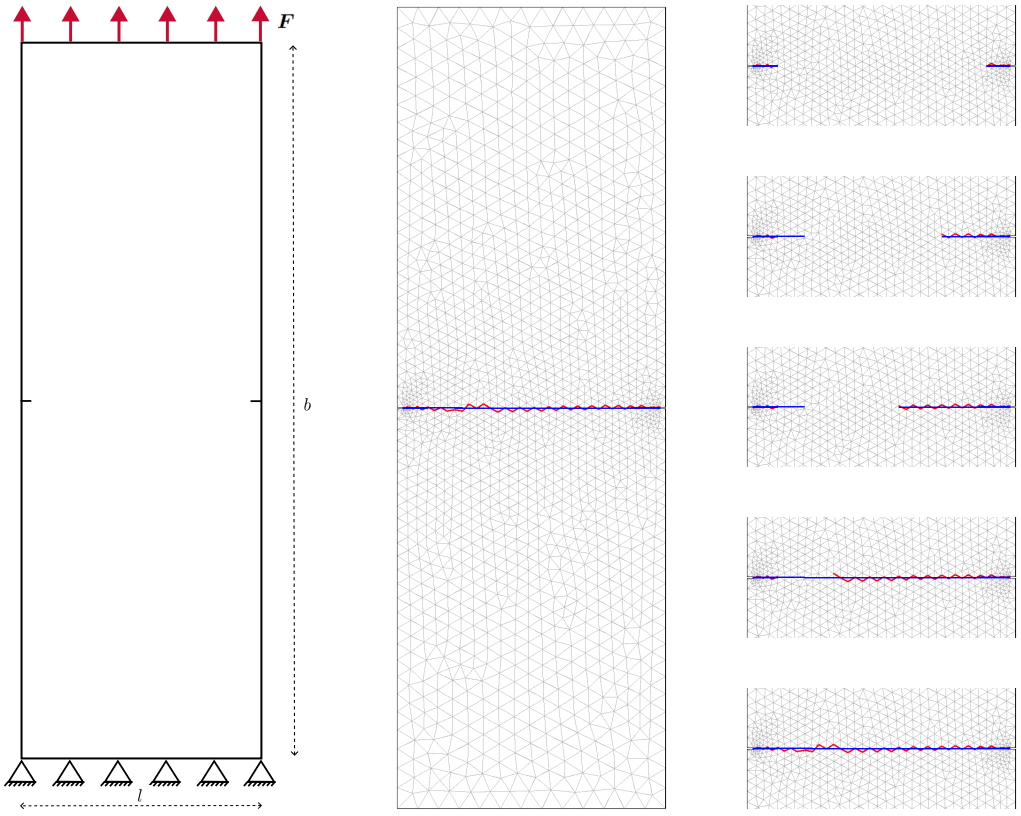

Figure 4.12: Results of the DENT test for the reduced SFM with the implemented additional features. On the left, the geometry and setup of the DENT test are shown. The middle presents the crack (blue) and surrogate crack (red) paths, while the right shows the crack paths at different loading stages of the simulation.

From Figure 4.12, it can be observed that the crack path follows a perfectly horizontal line. The crack propagation during different loading stages is shown on the right side of the figure. The simulation results indicate that two crack tips initiate simultaneously at the tips of both notches. As the loading increases, the cracks propagate towards each other, with the crack on the right side propagating slightly earlier than the crack on the left side. Eventually, the crack tips are close enough to merge, forming a single final crack.

5 Discussion

The results of this study show that the shifted fracture method (SFM) significantly improves the prediction of crack propagation in basic test cases compared to the Ortiz model. However, some challenges remain in applying the SFM to complex materials such as fiber-reinforced polymer (FRP) composites. The reduced SFM implementation, which builds upon the Ortiz model by only adding the area correction term and crack propagation algorithm from the SFM framework, showed very accurate results in the compact tension (CT) test, while the mesh dependency was reduced. Therefore, this model was preferred over the use of the full SFM implementation for subsequent evaluations, also because of the convergence issues regarding the full SFM. In curved crack path scenarios, the four-point bending test (FPBT) showed that the reduced SFM could successfully predict crack propagation. However, in the L-shape panel test, the same model led to convergence issues. While other studies using the stress intensity factor (SIF) criterion obtained stable results. To fully investigate whether the area correction term alone can improve mesh dependency and overall accuracy an extended Ortiz model was tested. This version extends the Ortiz model by only adding the area correction term. Unfortunately, this model appeared to be inaccurate and led to premature termination of the simulation. To address the challenges in applying the SFM to FRP composites, additional features were implemented. These features showed promising results in enhancing the SFM's applicability to FRP composites. Overall, this research shows that the reduced SFM implementation provides a robust, computationally efficient, and mesh-independent alternative to the Ortiz model in basic test cases. However, further improvements are needed to enhance its performance in complex geometries and FRP composites.

5.1. Interpretation of findings

5.1.1. Verification and validation of the SFM

Three numerical tests were performed to verify and validate the SFM: the CT test, the L-shape panel test, and the FPBT. With these tests, the full SFM, the reduced SFM, and the Ortiz model were evaluated on the ability to accurately predict crack propagation.

The CT test provided insights into mesh dependency, convergence behavior, and numerical accuracy. The full SFM showed highly accurate results with almost no mesh dependency, even for coarser meshes. Also, the load-displacement curves were consistent across the different mesh sizes, further supporting this conclusion. The observed high convergence of dissipated energy error aligns well with findings from the original SFM paper [15, 16]. This shows that the SFM can provide stable and accurate crack propagation predictions even with coarser meshes, reducing computational costs while maintaining accuracy.

Interestingly, the reduced SFM produced nearly identical results to the full SFM despite the fact that certain correction terms were left out. This suggests that for simpler crack paths (such as the CT test), the area correction term and the crack propagation algorithm alone are sufficient to correct mesh dependency issues. This also aligns with the findings of the SFM literature on the area correction term, which emphasizes that an accurate representation of the true fracture surface area is a key factor in reducing mesh dependency. However, the similarity observed between the reduced SFM to the full SFM raises an important question: under what conditions are the additional correction terms

necessary? While the tests show that they may not be necessary for simple test cases, maybe they are important for more complex scenarios.

The Ortiz model showed severe mesh dependency in both the crack paths and load-displacement curves. Because the model is an inter-element cracking method, cracks can only propagate along the element boundaries of the finite element mesh. For coarser mesh sizes, this leads to inaccurate results. This behavior is well-documented in literature [10], and the results reaffirm this. The Ortiz model requires finer meshes to achieve accurate results, which significantly increases computational cost.

One unexpected observation in the CT test was the unloading effects in the Ortiz model and the reduced SFM at coarse mesh sizes, whereas the full SFM experienced sudden vertical jumps in the equilibrium path. Since these effects disappeared with mesh refinement, it is likely that the coarse mesh did not sufficiently resolve the cohesive zone [1], leading to instability in equilibrium iterations. In literature, [25] similar staircase-like trends have been reported for cohesive zone modeling with coarser meshes, which supports this explanation. These results suggest that even though the SFM improves mesh independence, very coarse meshes may still introduce numerical artifacts, which should be considered in practical applications.

The L-shape panel test introduces a curved crack path, which adds complexity to the evaluation of crack propagation accuracy. The reduced SFM was able to accurately predict the initial stage of crack propagation in both mesh sizes, confirming that the area correction term effectively reduces mesh dependency, as observed in previous tests. However, after propagating a certain distance, convergence issues led to premature termination. The XFEM simulations by Dumstorff and Meschke [24], which also used the maximum principal tensile stress criterion for selecting the crack propagation direction, produced nearly identical results. This indicates that the criterion for crack propagation direction is probably the problem. However, the SFM implementation in the original paper used a stress intensity factor (SIF) criterion and successfully predicted crack paths. This highlights the importance of the choice of crack propagation direction.

This behavior can be explained as follows: In the L-shape panel test, there is a strong difference in stress distribution between the upper and lower regions of the material parallel to the crack. This leads to incorrect averaged stresses, which in turn affects the predicted crack direction [25]. The test highlights significant Mode II components, which explains why the maximum principal tensile stress criterion does not perform well. Because the criterion propagates perpendicular to the highest tensile stress and works therefore effectively when Mode I is dominant. Consequently, the criterion fails in this case because it neglects the shear stresses that influence crack propagation [15]. Future research should explore whether adopting the SIF criterion or alternative crack propagation criteria could resolve the observed issues.

The Ortiz model showed again mesh dependency in the L-shape panel test. The deviation from the reference crack path, particularly for the coarse mesh, shows the limitation of accurately predicting crack propagation in coarse meshes. The load-displacement curves further highlight this limitation, as peak loads in coarse meshes deviate substantially from reference solutions.

The FPBT, which also produces a curved crack path, showed that the reduced SFM produced highly accurate results in both the crack path and load-displacement curves. This shows that the reduced SFM can perform well for curved crack paths. However, unlike in the L-shape panel test, the reduced SFM failed to simulate crack propagation. This can likely be explained by the fact that the FPBT is primarily driven by Mode I fracture, with minimal shear (Mode II) effects. The stress field in the FPBT is more symmetric, reducing stress variations parallel to the crack and making the maximum principal tensile stress criterion more suitable for this case.

5.1.2. Performance of the extended Ortiz model

The results of the extended Ortiz model (Ortiz model + area correction term) showed that the model was ineffective in accurately predicting crack paths. It was observed that the crack paths of both mesh sizes, coarse and fine, deviated from the reference solution. The Ortiz model was also plotted for comparison, which was accurate for the fine mesh but inaccurate for the coarse mesh. The only difference between the two models is the addition of the area correction term implemented in the extended Ortiz model. This suggests that while the area correction term helps mitigate mesh dependency by improving

energy conservation [15], it alone does not sufficiently control crack propagation. Additional corrective mechanisms, such as the crack propagation algorithm included in the reduced SFM, are necessary to achieve accurate results.

However, another possible explanation for this issue could be that the area correction term is incorrectly calculated. Specifically, the normal vector to the crack direction is only calculated once at the initiation of a particular cohesive element and remains unchanged throughout the entire simulation. When a middle edge node of an element reaches the cohesive strength, the normal vector to the crack direction is calculated by using the maximum principal tensile stress criterion for that specific node. If this calculation is wrong, it can result in systematic inaccuracies in crack propagation. Therefore, this issue will not disappear with mesh refinement.

Despite these limitations, the potential of this approach remains promising. The reduced SFM already showed high accuracy with the area correction term, suggesting that improvements in its implementation could enhance the performance of the extended Ortiz model. Also, the extended Ortiz model has the same computational complexity as the Ortiz model but with the potential to be mesh-independent. Future research should investigate potential refinements in this method.

5.1.3. Impact of additional features

In Section 3.2, it became clear that several challenges exist in applying the SFM to FRP composites. To address these challenges, the following features were implemented in the reduced SFM: crack initialization, crack merging, and crack termination at boundaries. However, additional challenges, such as crack branching, cracking along curved paths, and others, remain open for future research.

Both the CT test and the DENT test demonstrated that the implemented features in the reduced SFM yielded accurate results in basic test cases. This suggests that the reduced SFM and also the full SFM have the potential for a more comprehensive implementation, making it suitable for more complex materials such as FRP composites.

Two important observations could be observed from the results. First, regarding the location of crack initialization. For simplicity, the Ortiz model's crack initialization approach was adopted and implemented in the reduced SFM. However, this approach is restricted to middle edge nodes of triangular elements. This resulted in an initial crack tip that did not correspond to the theoretical initial crack tip. Future studies could explore alternative criteria that allow crack initiation across the entire domain to enhance the method's flexibility. Nonetheless, the results indicate that the Ortiz model's crack initialization approach is compatible with the SFM framework. The second observation regards the DENT test. It was observed that the crack on the right side of the specimen propagated faster than the crack on the left side. A possible explanation for this asymmetry is that the mesh was not identical on both sides, resulting in slight differences in stress distribution. This caused one crack tip to reach the cohesive strength earlier than the other.

5.2. Limitations

As with any research, the results can be affected by certain limitations. Below, the main limitations are discussed, along with their impact on the study and possible solutions.

- **Complexity and limited documentation of the SFM:** The SFM introduces several new concepts, which initially took some time to fully understand and implement the method. The method itself was not overly complex in terms of computational structures, but the lack of detailed documentation, such as the absence of the discretized form of the variational equations, led to challenges. As a result, certain components, such as the tangential stiffness matrix contributions of the additional correction terms, were excluded from the implementation. While this omission did not affect the accuracy of the results, it increased the computational cost due to slower convergence.
- **Computational costs and hardware limitations:** Computational costs formed a major limitation in this study. In particular, performing simulations with complex fracture scenarios required more computational power than the available hardware could provide. Due to the limited computing power, it was impossible to execute even more complex fracture scenarios or large-scale simulations. Although sufficient results were obtained to draw valuable conclusions, this limits the breadth of validation and makes the conclusions less robust. For future research, this could easily be addressed by using more powerful computing resources.

- **Sensitivity of the crack direction criterion:** In this study, the maximum principal tensile stress criterion was chosen to determine the crack direction. This criterion is easy to implement and computationally efficient but has its limitations. In some simulations, such as the L-shaped panel test, which involves a mixed-mode fracture scenario, the criterion led to premature termination of the simulation. On the other hand, it performed well in the FPBT test, where mode I crack propagation is dominant. The original SFM paper suggested using the stress intensity factor (SIF) criterion for such cases, but its implementation was beyond the scope of this study due to time constraints and its computational complexity. This limitation indicates that the accuracy of the reduced SFM is influenced by the fracture mode, and future work should explore more robust criteria.
- **Challenges with the extended Ortiz model:** The idea of the extended Ortiz model was to develop a model with similar computational complexity as the Ortiz model but with reduced mesh dependency due to the implementation of the area correction term. However, errors in the calculation of this correction term led to inaccurate results. As a result, a decision had to be made: either dedicate more time to debugging the extended Ortiz model or shift focus back to the reduced SFM to address the challenges related to FRP composites. Eventually, the latter approach was chosen, which led to valuable insights, but at the cost of missing certain findings that could have been obtained from the extended Ortiz model.
- **Applicability of the reduced SFM to FRP composites:** The proposed SFM framework is currently only suitable for basic test scenarios and cannot be directly applied to complex structures such as FRP composites. Section 3.2 discusses the challenges that must be addressed to make the model suitable for such applications. Although some of these challenges were successfully addressed in this study, many others remain unresolved. As a result, the main research question, "How effective is the proposed method for arbitrary crack growth in predicting the propagation of cracks in fiber-reinforced polymer composites?" could not be fully answered. Future research will need to focus on addressing and validating these challenges.

5.3. Recommendations and future research

The results and limitations of this research provide valuable insights that can be used to further improve and expand the research. This section first presents recommendations aimed at directly improving the method and its implementation. Subsequently, broader directions for future research are discussed, focusing on realizing the full potential of the SFM and addressing the central research question.

5.3.1. Recommendations

Based on the results and limitations of this study, the following recommendations are made:

- **Choice of crack direction criterium:** The use of the maximum principal stress criterion is recommended for scenarios where mode I fracture is dominant. For mixed-mode crack scenarios, it is advisable to use a different criterion that also accounts for shear stresses, such as the stress intensity factor (SIF), as proposed in the original SFM publication [15]. This could significantly improve the reliability of the results in such cases.
- **Revisiting the extended Ortiz model:** It is recommended to reevaluate the implementation of the extended Ortiz model. The focus should be on determining whether the observed inaccuracies are due to implementation errors or fundamental limitations of the method. This model has the same computational complexity as the original Ortiz model but offers the potential to reduce mesh dependency. This could contribute to lower computational costs for coarser meshes, making large-scale simulations more accessible.
- **Refining the implemented additional features:** It is important to further validate and refine the additional features of the reduced SFM that were designed for FRP composites. Although these features have been successfully tested in simple scenarios, they also need to be examined in more complex crack situations. Additionally, the crack initiation feature, which is currently limited to middle edge nodes or elements, could be adapted to allow cracks to initiate anywhere in the domain. This could enhance the flexibility and applicability of the model.

- **Full implementation of the tangential stiffness matrices:** The proper implementation of the tangential stiffness matrix contributions is essential for the full implementation of the SFM. This would not only enable faster convergence but also make larger and more complex test cases feasible. While the current study worked with the reduced SFM, which is not affected by this, fully implementing these contributions would further strengthen and validate the full SFM implementation.

5.3.2. Future research

In addition to the recommendations, this study offers some directions for future research that can further develop the potential of the SFM:

- **Further development of the reduced SFM for FRP composites:** The potential of the reduced SFM is promising, especially in combination with an improved crack propagation algorithm. If the remaining challenges in applying the SFM to FRP composites are addressed, the method could evolve into a computationally efficient, mesh-independent solution for predicting crack growth in FRP composites. This is particularly relevant given the multiscale nature of FRP composites, where microscale simulations are essential for understanding fiber-matrix interactions and progressive failure behavior.
- **Integration into a multiscale fracture analysis framework:** An important long-term goal would be to integrate the reduced SFM into a fully coupled multiscale fracture analysis framework [1]. This framework would enable simulations that link microscale failure mechanisms to structural behavior at the macroscopic level. This could significantly improve both the accuracy of predictions and computational efficiency.
- **Fully addressing the main research question:** With the aforementioned recommendations and improvements, it should be possible to fully address the main research question of this study, “How effective is the proposed method for arbitrary crack growth in predicting the propagation of cracks in fiber-reinforced polymer composites?”. This would provide a valuable contribution to the field and enable practical applications for FRP composites.

6 Conclusion

The objective of this research project was to implement and evaluate the shifted fracture method (SFM), compare it with the Ortiz model, and assess its effectiveness for fiber-reinforced polymer (FRP) composites. The results show that the SFM, particularly the reduced SFM, provides several advantageous improvements over the Ortiz model for predicting crack propagation. The reduced SFM has proven to be a robust, computationally efficient, and mesh-independent alternative in basic fracture tests. However, its effectiveness in accurately predicting complex fracture processes in FRP composites remains a challenge.

The most important finding of this research is the importance of the area correction term in reducing mesh dependency. The results of the reduced SFM, which builds on the Ortiz model and implements only the area correction term and crack propagation algorithm while omitting other elements of the full SFM, emphasize this importance. This was also shown in both the compact tension (CT) test and the four-point bending tests (FPBT). The L-shaped panel test showed a limitation in the used crack direction criterion, the maximum principal stress criterion. This criterion failed to predict accurate crack paths under mixed-mode fracture conditions. This highlights the need for a more reliable crack direction criterion for mixed-mode fracture problems.

The extended Ortiz model, which includes only the area correction term in combination with the Ortiz model, was also tested. Although it couldn't accurately predict crack propagation, it demonstrated potential due to the high accuracy of the area correction term and the reduced complexity of the model. This indicates that further refinement of this model could be promising.

The newly implemented features for applying the SFM to FRP composites have shown promising results in basic fracture tests. Nevertheless, additional validation and improvement are required to comprehensively evaluate the SFM's applicability in complex fracture situations involving FRP composites. A fully developed, mesh-independent SFM framework could significantly reduce computational costs while maintaining accuracy in crack propagation predictions. If this could be successfully integrated into a multiscale modeling framework, the SFM could be a useful tool for fracture analysis in engineering applications.

This research has clearly demonstrated the strengths and weaknesses of the SFM. It has shown, in particular, that the method effectively reduces mesh dependency, making it a very promising and computationally efficient method as a fracture framework. It also showed that the reduced SFM, which has lower computational complexity than the full SFM, can be used for accurate prediction of arbitrary crack propagation. However, the study also indicates that improvements are needed in the selection of the crack direction criterion and in the validation of more complex fracture scenarios. These insights provide a solid foundation for future research to enhance the SFM and make it applicable to more advanced materials, such as FRP composites.

References

[1] F. P. van der Meer. “Mesolevel Modeling of Failure in Composite Laminates: Constitutive, Kinematic and Algorithmic Aspects”. In: *Archives of Computational Methods in Engineering: State of the Art Reviews* 19.3 (2012), pp. 381–425. DOI: 10.1007/s11831-012-9076-y.

[2] Dragan Kovačević, Bharath K. Sundararajan, and Frans P. van der Meer. “Microscale modeling of rate-dependent failure in thermoplastic composites under off-axis loading”. In: *Engineering Fracture Mechanics* 276 (2022), p. 108884. ISSN: 0013-7944. DOI: https://doi.org/10.1016/j.engfracmech.2022.108884.

[3] G.T. Camacho and M. Ortiz. “Computational modelling of impact damage in brittle materials”. In: *International Journal of Solids and Structures* 33.20 (1996), pp. 2899–2938. ISSN: 0020-7683. DOI: https://doi.org/10.1016/0020-7683(95)00255-3.

[4] T.S. Hille, A.S.J. Suiker, and S. Turteltaub. “Microcrack nucleation in thermal barrier coating systems”. In: *Engineering Fracture Mechanics* 76.6 (2009), pp. 813–825. ISSN: 0013-7944. DOI: https://doi.org/10.1016/j.engfracmech.2008.12.010.

[5] “5 - Fiber-reinforced polymer types and properties”. In: *Advanced Fiber-Reinforced Polymer(FRP) Composites for Structural Applications (Second Edition)*. Ed. by Jiping Bai. Second Edition. Woodhead Publishing Series in Civil and Structural Engineering. Woodhead Publishing, 2023, pp. 93–99. ISBN: 978-0-12-820346-0. DOI: https://doi.org/10.1016/B978-0-12-820346-0.00014-9.

[6] D.S. Dugdale. “Yielding of steel sheets containing slits”. In: *Journal of the Mechanics and Physics of Solids* 8.2 (1960), pp. 100–104. ISSN: 0022-5096. DOI: https://doi.org/10.1016/0022-5096(60)90013-2.

[7] G.I. Barenblatt. “The Mathematical Theory of Equilibrium Cracks in Brittle Fracture”. In: ed. by H.L. Dryden et al. Vol. 7. Advances in Applied Mechanics. Elsevier, 1962, pp. 55–129. DOI: https://doi.org/10.1016/S0065-2156(08)70121-2.

[8] C.T. Sun and Z.-H. Jin. “Chapter 9 - Cohesive Zone Model”. In: *Fracture Mechanics*. Ed. by C.T. Sun and Z.-H. Jin. Boston: Academic Press, 2012, pp. 227–246. ISBN: 978-0-12-385001-0. DOI: https://doi.org/10.1016/B978-0-12-385001-0.00009-2.

[9] Timon Rabczuk. “Computational Methods for Fracture in Brittle and Quasi-Brittle Solids: State-of-the-Art Review and Future Perspectives”. In: *International Scholarly Research Notices* 2013.1 (2013), p. 849231. DOI: https://doi.org/10.1155/2013/849231.

[10] Jeong-Hoon Song, Hongwu Wang, and Ted Belytschko. “A comparative study on finite element methods for dynamic fracture”. In: *Computational Mechanics* 42.2 (2008), pp. 239–250. ISSN: 1432-0924. DOI: 10.1007/s00466-007-0210-x.

[11] F. P. van der Meer and L. J. Sluys. “A phantom node formulation with mixed mode cohesive law for splitting in laminates”. In: *International Journal of Fracture* 158.2 (2009), pp. 107–124. ISSN: 1573-2673. DOI: 10.1007/s10704-009-9344-5. URL: https://doi.org/10.1007/s10704-009-9344-5.

[12] Y. Liu et al. “Modeling of dynamic mode I crack growth in glass fiber-reinforced polymer composites: fracture energy and failure mechanism”. In: *Engineering Fracture Mechanics* 243 (2021), p. 107522. ISSN: 0013-7944. DOI: https://doi.org/10.1016/j.engfracmech.2020.107522.

[13] R. de Borst et al. *Computational Methods in Non-Linear Solid Mechanics: CTme5142: Dictaat Behorende Bij College CT5142*. TU Delft, 1999.

[14] Miguel A. Gutiérrez. “Energy release control for numerical simulations of failure in quasi-brittle solids”. In: *Communications in Numerical Methods in Engineering* 20.1 (2004), pp. 19–29. DOI: https://doi.org/10.1002/cnm.649.

[15] Kangan Li et al. “The shifted fracture method”. In: *International Journal for Numerical Methods in Engineering* 122.22 (2021), pp. 6641–6679. DOI: https://doi.org/10.1002/nme.6806.

[16] Kangan Li, Antonio Rodríguez-Ferran, and Guglielmo Scovazzi. “The simple shifted fracture method”. In: *International Journal for Numerical Methods in Engineering* 124.12 (2023), pp. 2837–2875. DOI: https://doi.org/10.1002/nme.7232.

[17] Alberto Carpinteri and Giovanni Colombo. “Numerical analysis of catastrophic softening behaviour (snap-back instability)”. In: *Computers and Structures* 31.4 (1989), pp. 607–636. ISSN: 0045-7949. DOI: https://doi.org/10.1016/0045-7949(89)90337-4.

[18] Nicolas Moës, John Dolbow, and Ted Belytschko. “A finite element method for crack growth without remeshing”. In: *International Journal for Numerical Methods in Engineering* 46.1 (1999), pp. 131–150. DOI: https://doi.org/10.1002/(SICI)1097-0207(19990910)46:1<131::AID-NME726>3.0.CO;2-J.

[19] C.A. Duarte, I. Babuška, and J.T. Oden. “Generalized finite element methods for three-dimensional structural mechanics problems”. In: *Computers and Structures* 77.2 (2000), pp. 215–232. ISSN: 0045-7949. DOI: https://doi.org/10.1016/S0045-7949(99)00211-4.

[20] Vinh Phu Nguyen. “Discontinuous Galerkin/extrinsic cohesive zone modeling: Implementation caveats and applications in computational fracture mechanics”. In: *Engineering Fracture Mechanics* 128 (2014), pp. 37–68. ISSN: 0013-7944. DOI: https://doi.org/10.1016/j.engfracmech.2014.07.003.

[21] Oriol Colomés et al. *Finite Elements in Civil Engineering and Geosciences*. Accessed: 6 Jan 2025. 2023. URL: https://interactivetextbooks.citg.tudelft.nl/computational-modelling/intro.html#finite-elements-in-civil-engineering-and-geosciences.

[22] Dynaflow Research Group. *Developing Numerical Programs with Jem and Jive*. PowerPoint slides. Accessed: 6 Jan 2025. n.d. URL: https://dynaflow.com/software/jive/jive-downloads/.

[23] David C. Lay, Steven R. Lay, and Judi J. McDonald. *Linear Algebra and Its Applications, Global Edition*. Pearson Education, Limited, 2015.

[24] Peter Dumstorff and Günther Meschke. “Crack propagation criteria in the framework of X-FEM-based structural analyses”. In: *International Journal for Numerical and Analytical Methods in Geomechanics* 31.2 (2007), pp. 239–259. DOI: https://doi.org/10.1002/nag.560.

[25] Jörg F. Unger, Stefan Eckardt, and Carsten Könke. “Modelling of cohesive crack growth in concrete structures with the extended finite element method”. In: *Computer Methods in Applied Mechanics and Engineering* 196.41 (2007), pp. 4087–4100. ISSN: 0045-7825. DOI: https://doi.org/10.1016/j.cma.2007.03.023.

[26] B. J. Winkler. *Traglastuntersuchungen von unbewehrten und bewehrten Betonstrukturen auf der Grundlage eines objektiven Werkstoffgesetzes für Beton*. Innsbruck: Innsbruck University Press, 2001.

[27] Nicolas Moës and Ted Belytschko. “Extended finite element method for cohesive crack growth”. In: *Engineering Fracture Mechanics* 69.7 (2002), pp. 813–833. ISSN: 0013-7944. DOI: https://doi.org/10.1016/S0013-7944(01)00128-X.

[28] A. Carpinteri et al. “Is mode II fracture energy a real material property?” In: *Computers and Structures* 48.3 (1993), pp. 397–413. ISSN: 0045-7949. DOI: https://doi.org/10.1016/0045-7949(93)90316-6.

[29] Kangan Li, Antonio Rodríguez-Ferran, and Guglielmo Scovazzi. “Crack branching and merging simulations with the shifted fracture method”. In: *Computer Methods in Applied Mechanics and Engineering* 433 (2025), p. 117528. ISSN: 0045-7825. DOI: https://doi.org/10.1016/j.cma.2024.117528.

[30] Jiping Bai. “1 - Introduction”. In: *Advanced Fiber-Reinforced Polymer(FRP) Composites for Structural Applications (Second Edition)*. Ed. by Jiping Bai. Second Edition. Woodhead Publishing Series in Civil and Structural Engineering. Woodhead Publishing, 2023, pp. 1–6. ISBN: 978-0-12-820346-0. DOI: https://doi.org/10.1016/B978-0-12-820346-0.00013-7.

[31] Alak Kumar Patra, Indrajit Ray, and J. S. Alein. “Introduction to Fracture Failure Analysis of Fiber Reinforced Polymer Matrix Composites”. In: *Fracture Failure Analysis of Fiber Reinforced Polymer Matrix Composites*. Ed. by Sanjay Mavinkere Rangappa et al. Singapore: Springer Singapore, 2021, pp. 1–25. ISBN: 978-981-16-0642-7. DOI: 10.1007/978-981-16-0642-7_1.

[32] Dragan Kovačević, Bharath K. Sundararajan, and Frans P. van der Meer. “Micromechanical model for off-axis creep rupture in unidirectional composites undergoing finite strains”. In: *Composites Part A: Applied Science and Manufacturing* 176 (2024), p. 107860. ISSN: 1359-835X. DOI: https://doi.org/10.1016/j.compositesa.2023.107860.

[33] C.T. Sun and Z.-H. Jin. “Chapter 3 - The Elastic Stress Field around a Crack Tip”. In: *Fracture Mechanics*. Ed. by C.T. Sun and Z.-H. Jin. Boston: Academic Press, 2012, pp. 25–75. ISBN: 978-0-12-385001-0. DOI: https://doi.org/10.1016/B978-0-12-385001-0.00003-1.

A

Linearized discrete form of the SFM

To implement the shifted fracture method (SFM) into the in-house finite element code, the derived shifted weak form equations (see section 2.4.2) must be rewritten to a linearized discrete form. This can be done by a reinterpretation of the left-hand side of the discrete form as an equilibrium between internal and external forces. [21]

The starting point is the expression for the shifted weak form derived in Section 2.4.2 (Eq. 2.32):

$$\begin{aligned} &\int_\Omega \nabla^s \mathbf{w} : \boldsymbol{\sigma} \ \mathrm{d}\Omega + \int_{\tilde{\Gamma}_c} [\![\mathbf{w}]\!] \cdot (\tilde{\mathbf{n}} \cdot \mathbf{n}) \mathbf{t}_{\mathsf{coh}}(\mathbf{w}(\mathbf{u})) \ \mathrm{d}\Gamma \\ &+ \int_{\tilde{\Gamma}_c} [\![\mathbf{w}]\!] \cdot \{\!\{\boldsymbol{\sigma}(\mathbf{u})\}\!\} (\tilde{\mathbf{n}} - (\tilde{\mathbf{n}} \cdot \mathbf{n})\mathbf{n}) \ \mathrm{d}\Gamma + \int_{\tilde{\Gamma}_c} \{\!\{\mathbf{w}\}\!\} \cdot [\![\boldsymbol{\sigma}(\mathbf{u})]\!] (\tilde{\mathbf{n}} - (\tilde{\mathbf{n}} \cdot \mathbf{n})\mathbf{n}) \ \mathrm{d}\Gamma \\ &= \int_\Omega \mathbf{w} \cdot \mathbf{b} \ \mathrm{d}\Omega + \int_{\Gamma_N} \mathbf{w} \cdot \bar{\mathbf{t}} \ \mathrm{d}\Gamma \quad \forall \quad \mathbf{w} \end{aligned} \tag{A.1}$$

The same weak form can also be derived by using the virtual work principle, which can be obtained by substituting $\mathbf{w}$ for a virtual displacement $\boldsymbol{\delta}\mathbf{u}$. By doing this, the weak form can be divided into two terms with clear physical interpretation, in which the gradient of a virtual displacement can be seen as a virtual strain $\nabla^s \boldsymbol{\delta}\mathbf{u} = \boldsymbol{\delta\varepsilon}$:

$$\begin{aligned} &\underbrace{\int_\Omega \nabla^s \boldsymbol{\delta}\mathbf{u} : \boldsymbol{\sigma}(\mathbf{u}) \ \mathrm{d}\Omega + \int_{\tilde{\Gamma}_c} [\![\boldsymbol{\delta}\mathbf{u}]\!] \cdot (\tilde{\mathbf{n}} \cdot \mathbf{n}) \cdot \mathbf{t}_{\mathsf{coh}}(\mathbf{w}(\mathbf{u} + \nabla\mathbf{u}\,\mathbf{d})) \ \mathrm{d}\Gamma}_{W_{\mathsf{int}}} \\ &\underbrace{+ \int_{\tilde{\Gamma}_c} [\![\boldsymbol{\delta}\mathbf{u}]\!] \cdot \{\!\{\boldsymbol{\sigma}(\mathbf{u})\}\!\} \cdot (\tilde{\mathbf{n}} - (\tilde{\mathbf{n}} \cdot \mathbf{n})\mathbf{n}) \ \mathrm{d}\Gamma + \int_{\tilde{\Gamma}_c} \{\!\{\boldsymbol{\delta}\mathbf{u}\}\!\} \cdot [\![\boldsymbol{\sigma}(\mathbf{u})]\!] \cdot (\tilde{\mathbf{n}} - (\tilde{\mathbf{n}} \cdot \mathbf{n})\mathbf{n}) \ \mathrm{d}\Gamma}_{W_{\mathsf{int}}} \\ &\underbrace{- \int_\Omega \boldsymbol{\delta}\mathbf{u} \cdot \mathbf{b} \ \mathrm{d}\Omega - \int_{\Gamma_N} \boldsymbol{\delta}\mathbf{u} \cdot \mathbf{t} \ \mathrm{d}\Gamma}_{W_{\mathsf{ext}}} = 0, \quad \forall \quad \boldsymbol{\delta}\mathbf{u} \end{aligned} \tag{A.2}$$

The above equation can be seen as a balance between internal work driven through deformation and external work related to the loads applied to the body. To obtain the discrete form, the following approximations can be introduced:

$$\begin{aligned} \delta\mathbf{u} &= \mathbf{N}\delta\mathbf{a}, & [\![\delta\mathbf{u}]\!] &= \delta\mathbf{u}^+ - \delta\mathbf{u}^- = \mathbf{N}^{\mathsf{int}}(\delta\mathbf{a}^+ - \delta\mathbf{a}^-), \\ \boldsymbol{\delta\varepsilon} &= \mathbf{B}\delta\mathbf{a}, & \{\!\{\delta\mathbf{u}\}\!\} &= \frac{1}{2}(\delta\mathbf{u}^+ + \delta\mathbf{u}^-) = \frac{1}{2}\mathbf{N}^{\mathsf{int}}(\delta\mathbf{a}^+ + \delta\mathbf{a}^-). \end{aligned}$$

where $\mathbf{N}^{\mathsf{int}}$ is the matrix of the interface shape functions, and $\mathbf{N}$ is the matrix of the bulk element shape functions. Using the linear algebra operation $(\mathbf{AB})^{\mathrm{T}} = \mathbf{B}^{\mathrm{T}}\mathbf{A}^{\mathrm{T}}$ to remove $\delta\mathbf{a}$ from the integrals, the

discrete form of the weak form can be obtained:

$$\begin{aligned}
&\underbrace{\int_\Omega \mathbf{B}^{\mathrm{T}}\sigma(\mathbf{u})\ \mathrm{d}\Omega}_{f_{\text{int}}} \\
&\underbrace{+\int_{\tilde{\Gamma}_c}(\mathbf{N}^{\text{int}})^{\mathrm{T}}(\tilde{\mathbf{n}}\cdot\mathbf{n})\mathbf{t}_{\text{coh}}(\mathbf{w}(\mathbf{u}+\nabla\mathbf{u}\mathbf{d}))\mathrm{d}\Gamma-\int_{\tilde{\Gamma}_c}(\mathbf{N}^{\text{int}})^{\mathrm{T}}(\tilde{\mathbf{n}}\cdot\mathbf{n})\mathbf{t}_{\text{coh}}(\mathbf{w}(\mathbf{u}+\nabla\mathbf{u}\mathbf{d}))\mathrm{d}\Gamma}_{f_{\text{int}}} \\
&\underbrace{+\int_{\tilde{\Gamma}_c}(\mathbf{N}^{\text{int}})^{\mathrm{T}}\left\{\!\!\left\{\sigma(\mathbf{u})\right\}\!\!\right\}(\tilde{\mathbf{n}}-(\tilde{\mathbf{n}}\cdot\mathbf{n})\mathbf{n})\ \mathrm{d}\Gamma-\int_{\tilde{\Gamma}_c}(\mathbf{N}^{\text{int}})^{\mathrm{T}}\left\{\!\!\left\{\sigma(\mathbf{u})\right\}\!\!\right\}(\tilde{\mathbf{n}}-(\tilde{\mathbf{n}}\cdot\mathbf{n})\mathbf{n})\ \mathrm{d}\Gamma}_{f_{\text{int}}} \\
&\underbrace{+\int_{\tilde{\Gamma}_c}(\mathbf{N}^{\text{int}})^{\mathrm{T}}[\![\sigma(\mathbf{u})]\!](\tilde{\mathbf{n}}-(\tilde{\mathbf{n}}\cdot\mathbf{n})\mathbf{n})\ \mathrm{d}\Gamma+\int_{\tilde{\Gamma}_c}(\mathbf{N}^{\text{int}})^{\mathrm{T}}[\![\sigma(\mathbf{u})]\!](\tilde{\mathbf{n}}-(\tilde{\mathbf{n}}\cdot\mathbf{n})\mathbf{n})\ \mathrm{d}\Gamma}_{f_{\text{int}}} \\
&\underbrace{=\int_\Omega \mathbf{N}^{\mathrm{T}}\mathbf{b}\ \mathrm{d}\Omega+\int_{\Gamma_N}\mathbf{N}^{\mathrm{T}}\bar{\mathbf{t}}\ \mathrm{d}\Gamma}_{f_{\text{ext}}}
\end{aligned} \tag{A.3}$$

From the definition of work, these terms must correspond to internal forces and external forces. The above equation represents the following system of equations:

$$\mathbf{f}_{\text{ext}}-\mathbf{f}_{\text{int,bulk}}(\mathbf{a})-\mathbf{f}_{\text{int,crack}}(\mathbf{a})=0 \tag{A.4}$$

where $\mathbf{f}_{\text{ext}}$ is the external force vector, $\mathbf{f}_{\text{int}}$ the internal force vector, which is composed of two parts, $\mathbf{f}_{\text{int,bulk}}$ from the bulk elements and $\mathbf{f}_{\text{int,crack}}$ from the crack interface which consist of three terms.

$$\mathbf{f}_{\text{int,bulk}}=\int_\Omega \mathbf{B}^{\mathrm{T}}\sigma(\mathbf{u})\ \mathrm{d}\Omega \tag{A.5}$$

$$\mathbf{f}_{\text{int,crack,1}}=\int_{\tilde{\Gamma}_c}(\mathbf{N}^{\text{int}})^{\mathrm{T}}(\tilde{\mathbf{n}}\cdot\mathbf{n})\mathbf{t}_{\text{coh}}(\mathbf{w}(\mathbf{u}+\nabla\mathbf{u}\mathbf{d}))\mathrm{d}\Gamma-\int_{\tilde{\Gamma}_c}(\mathbf{N}^{\text{int}})^{\mathrm{T}}(\tilde{\mathbf{n}}\cdot\mathbf{n})\mathbf{t}_{\text{coh}}(\mathbf{w}(\mathbf{u}+\nabla\mathbf{u}\mathbf{d}))\mathrm{d}\Gamma \tag{A.6}$$

$$\mathbf{f}_{\text{int,crack,2}}=\int_{\tilde{\Gamma}_c}(\mathbf{N}^{\text{int}})^{\mathrm{T}}\left\{\!\!\left\{\sigma(\mathbf{u})\right\}\!\!\right\}(\tilde{\mathbf{n}}-(\tilde{\mathbf{n}}\cdot\mathbf{n})\mathbf{n})\ \mathrm{d}\Gamma-\int_{\tilde{\Gamma}_c}(\mathbf{N}^{\text{int}})^{\mathrm{T}}\left\{\!\!\left\{\sigma(\mathbf{u})\right\}\!\!\right\}(\tilde{\mathbf{n}}-(\tilde{\mathbf{n}}\cdot\mathbf{n})\mathbf{n})\ \mathrm{d}\Gamma \tag{A.7}$$

$$\mathbf{f}_{\text{int,crack,3}}=\int_{\tilde{\Gamma}_c}(\mathbf{N}^{\text{int}})^{\mathrm{T}}[\![\sigma(\mathbf{u})]\!](\tilde{\mathbf{n}}-(\tilde{\mathbf{n}}\cdot\mathbf{n})\mathbf{n})\ \mathrm{d}\Gamma+\int_{\tilde{\Gamma}_c}(\mathbf{N}^{\text{int}})^{\mathrm{T}}[\![\sigma(\mathbf{u})]\!](\tilde{\mathbf{n}}-(\tilde{\mathbf{n}}\cdot\mathbf{n})\mathbf{n})\ \mathrm{d}\Gamma \tag{A.8}$$

$$\mathbf{f}_{\text{ext}}=\int_\Omega \mathbf{N}^{\mathrm{T}}\mathbf{b}\ \mathrm{d}\Omega+\int_{\Gamma_N}\mathbf{N}^{\mathrm{T}}\bar{\mathbf{t}}\ \mathrm{d}\Gamma \tag{A.9}$$

The nonlinear equations are solved with a Newton-Raphson method, which requires linearization of the terms in equation A.3 except the external force vector, which is independent of the displacements. The linearized form is:

$$\tilde{\mathbf{f}}_{int}(\mathbf{a})=\mathbf{f}_{int}(\mathbf{a}_0)+\frac{\partial\mathbf{f}_{int}}{\partial\mathbf{a}}(\mathbf{a}-\mathbf{a}_0) \tag{A.10}$$

where $\frac{\partial\mathbf{f}_{int}}{\partial\mathbf{a}}$ is the tangent stiffness matrix $\mathbf{K}$. Linearization of the internal force vector terms leads to

the following tangent stiffness matrices:

$$\mathbf{K}_{\text{bulk}} = \int_{\Omega} \mathbf{B}^{\mathrm{T}}\mathbf{C}\mathbf{B} \ \mathrm{d}\Omega \tag{A.11}$$

$$\mathbf{K}_{\text{crack,1}} = \int_{\Omega} (\mathbf{N}^{\text{int}})^{\mathrm{T}}\mathbf{R}^{\mathrm{T}}\frac{\partial \mathbf{t}}{\partial [\![\mathbf{u}]\!]}\mathbf{R}\mathbf{N}^{\text{int}}(\tilde{\mathbf{n}}\cdot\mathbf{n}) \ \mathrm{d}\Gamma - \int_{\Omega} (\mathbf{N}^{\text{int}})^{\mathrm{T}}\mathbf{R}^{\mathrm{T}}\frac{\partial \mathbf{t}}{\partial [\![\mathbf{u}]\!]}\mathbf{R}\mathbf{N}^{\text{int}}(\tilde{\mathbf{n}}\cdot\mathbf{n}) \ \mathrm{d}\Gamma \tag{A.12}$$

$$\begin{aligned}\mathbf{K}_{\text{crack,2}} = &\int_{\Omega} (\mathbf{N}^{\text{int}})^{\mathrm{T}}\frac{1}{2}(\mathbf{D}^1\mathbf{B}^1 + \mathbf{D}^2\mathbf{B}^2)(\tilde{\mathbf{n}} - (\tilde{\mathbf{n}}\cdot\mathbf{n})\mathbf{n}) \ \mathrm{d}\Gamma \\ &- \int_{\Omega} (\mathbf{N}^{\text{int}})^{\mathrm{T}}\frac{1}{2}(\mathbf{D}^1\mathbf{B}^1 + \mathbf{D}^2\mathbf{B}^2)(\tilde{\mathbf{n}} - (\tilde{\mathbf{n}}\cdot\mathbf{n})\mathbf{n}) \ \mathrm{d}\Gamma\end{aligned} \tag{A.13}$$

$$\begin{aligned}\mathbf{K}_{\text{crack,3}} = &\int_{\Omega} \frac{1}{2}(\mathbf{N}^{\text{int}})^{\mathrm{T}}(\mathbf{D}^1\mathbf{B}^1 - \mathbf{D}^2\mathbf{B}^2)(\tilde{\mathbf{n}} - (\tilde{\mathbf{n}}\cdot\mathbf{n})\mathbf{n}) \ \mathrm{d}\Gamma \\ &+ \int_{\Omega} \frac{1}{2}(\mathbf{N}^{\text{int}})^{\mathrm{T}}(\mathbf{D}^1\mathbf{B}^1 - \mathbf{D}^2\mathbf{B}^2)(\tilde{\mathbf{n}} - (\tilde{\mathbf{n}}\cdot\mathbf{n})\mathbf{n}) \ \mathrm{d}\Gamma\end{aligned} \tag{A.14}$$